Geodynamo simulations with vigorous convection and low viscosity

Nathanaël Schaeffer, Dominique Jault, Henri-Claude Nataf, Alexandre Fournier

Geodynamo simulations with vigorous convection and low viscosity

N. Schaeffer[1], D. Jault [1], H.-C. Nataf [1], A. Fournier[2]

[1] Univ. Grenoble Alpes, CNRS, ISTerre, *F-38000* Grenoble, France

[2] Institut de Physique du Globe de Paris, Sorbonne Paris Cité,
Univ. Paris Diderot, CNRS, 1 rue Jussieu, F-75005 Paris, France.

December 23, 2016

Abstract

Direct numerical simulations of the magnetohydrodynamics in a spherical shell have been widely used to study the internal magnetic field of the Earth. However, despite continuing progress, the regime in which these simulations operate is in many aspects still far from what is expected in the Earth's core. This undermines the confidence in scaling the simulation outputs to actual planetary cores.

In an attempt to reach further towards realistic regimes, we have produced a series of three geodynamo simulations with increasingly demanding parameters, lowering the viscosity while keeping a strong convective driving. The third and last simulation of our series has many parameters and diagnostics closer to the Earth's core than previous direct simulations. In particular the Ekman number $E = 10^{-7}$, the magnetic Prandtl number $Pm = 0.1$, the magnetic Reynolds number $Rm \gtrsim 500$. The magnetic energy dominates the kinetic energy by a factor 12.

We describe in details the mean fields, fluctuations, spectra, and dynamical balances, with an emphasis on spatio-temporal analysis. As the parameters become more and more Earth-like, we observe that ohmic heating becomes dominant in the energy dissipation budget. The cylinder tangent to the inner-core and aligned with the rotation axis appears as a sharp boundary between two regions of different dynamics. A strong zonal flow aligned with strong toroidal magnetic field occupies the inner region, where lighter fluid is trapped. This contrasts with the outer region, where the mean toroidal field is replaced by a strong poloidal field, which suppresses the mean zonal flow. There, we observe the emergence of large-scale eddies mostly invariant along the rotation axis, that drive a westward drift of the magnetic field near the equator. These slowly evolving and large scale flows are driven by the buoyancy of large-scale density anomalies, while faster fluctuations rely mostly on a balance between Laplace and Coriolis forces, even at large scales. Torsional waves are predominantly generated near the inner-core by Lorentz stress and propagate

outward. The fields are very heterogeneous: regions with strong magnetic field and large scale flow lie close to regions with almost no magnetic field where small-scale convection occurs.

We discuss our results, their relevance and possible implications for the Earth's core dynamics.

Contents

1 Introduction

Earth's magnetic field is generated by a turbulent flow of liquid metal in the core. The pioneering work of Glatzmaier and Roberts (1995) launched the first generation of numerical simulations of the geodynamo. For the first time, a self-sustained magnetic field was produced by a self-consistent convective geodynamo model. It exhibited several key

features of the Earth's magnetic field: a mostly dipolar field aligned with the rotation axis, and polarity reversals. These findings were somewhat surprising, considering the huge gap between the parameters used in the simulations and their expected values in the Earth's core.

Second generation numerical simulations of the geodynamo explored the parameter space and derived scaling laws (Christensen and Aubert, 2006). As the mean properties of the simulations could be cast in laws that excluded diffusion properties (viscosity, thermal and magnetic diffusivities), it was argued that the simulations had reached an asymptotic regime, which allowed extrapolation to the Earth (Christensen et al., 2010), planets (Christensen, 2010), and stars (Christensen et al., 2009).

Rapidly, several teams questioned that these simulations really reached an asymptotic regime, and that it was the right asymptotic regime for the Earth. Reanalyzing the large suite of simulations of Christensen and Aubert (2006), King and Buffett (2013) pointed out that viscous dissipation was far from negligible in the simulations, and that magnetic forces did not seem to play a major role, contrary to what is expected for the Earth's core; Cheng and Aurnou (2016) showed that the diffusionless scaling laws were hiding an actual dependency upon viscosity; Oruba and Dormy (2014) derived alternative scaling laws in which the magnetic field intensity depends upon viscosity and rotation rate.

In the mean time, new analyses of geomagnetic observations revealed several remarkable features (Gillet et al., 2015; Pais et al., 2015): the analysis of Pais and Jault (2008) yielded a large-scale off-centered quasi-geostrophic gyre around the inner core (also see: Schaeffer and Pais, 2011); Finlay and Jackson (2003) showed evidence for equatorial magnetic waves propagating at decadal time-scales; Gillet et al. (2010) discovered torsional oscillations, and derived the first measure of the intensity of the magnetic field inside the core from their propagation velocity. These discoveries highlighted that magnetic energy in the Earth's core is about 4 orders of magnitude larger than kinetic energy. They also prompted modelers to look for these signatures in their simulations.

Efforts in these directions revived the search for inviscid magnetostrophic dynamos (Livermore et al., 2013; Wu and Roberts, 2015). Taking an opposite approach, Dormy (2016) obtained strong-field dynamos for large Pm values. Increased computational power also made it possible to push the parameters toward more realistic values (Kageyama et al., 2008; Sakuraba and Roberts, 2009; Sheyko, 2014; Yadav et al., 2016b). Figure 1 displays the current parameter-space coverage that has been achieved by several groups. It shows that having a large magnetic Reynolds number Rm is difficult to achieve at low viscosity (low Ekman number E and low magnetic Prandtl number Pm – see definitions in section 2.1), because the flow becomes turbulent, implying that smaller and smaller scales need to be resolved, leading to tremendous computing costs. In contrast to direct simulations that are committed to resolve all dynamical scales, Aubert et al. (2017) have used a form of hyper-viscosity to kill the smallest scales while keeping the largest ones unaffected. This allowed them to reach very low values of the large-scale viscosity and argue for a continuous path connecting today's simulations with the Earth's core.

Here, we present an attempt to reach turbulent regime in direct numerical simulations of the geodynamo. By not artificially damping the smallest flow scales, we ensure unbiased

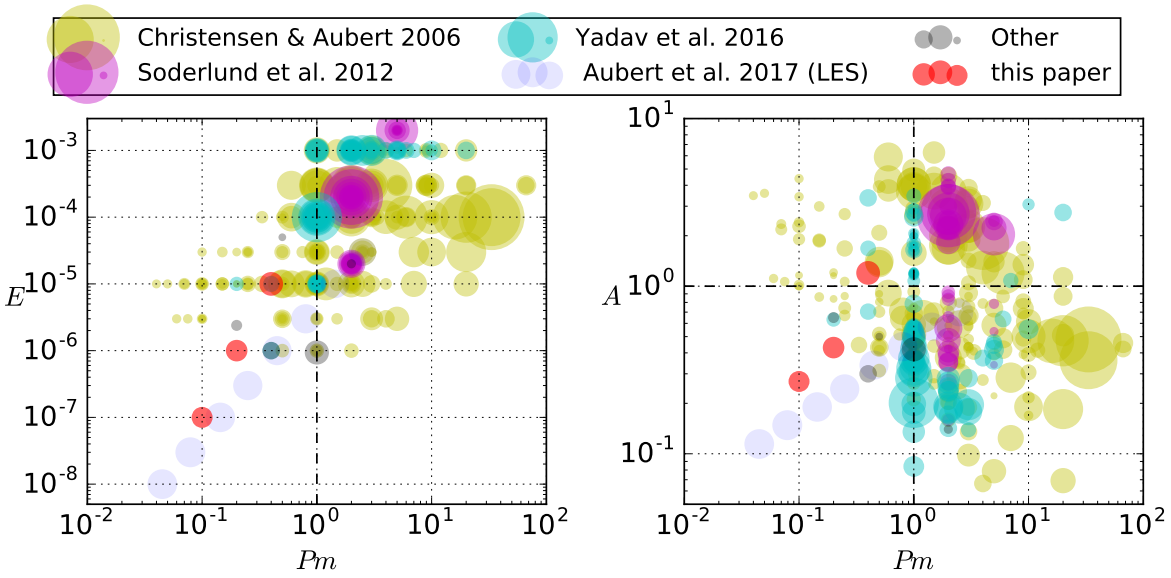

Figure 1: Some numerical simulations of the geodynamo represented in parameter space (E, Pm, Rm, A), with the surface of the discs being proportional to Rm. Our three simulations are shown in red. In each plot, the Earth's core lies far away beyond the bottom left corner (see table 1), out of reach from current models. Only few simulations achieve high Rm together with low viscosity (low E and low Pm). Similarly, few simulations lie in the low Pm, low A region. The data sets include the work of Christensen and Aubert (2006), Soderlund et al. (2012), Yadav et al. (2016a), the simulations with hyperviscosity and $Rm \simeq 1000$ of Aubert et al. (2017), and other simulations displayed in table 1.

dynamics at all scales.

We have been able to reach strongly forced dynamos at low viscosity, where the magnetic energy becomes larger than the kinetic energy. In this way, all *a priori* time-scales have the same ordering than what is inferred from observations. Fast and slow variations of the magnetic field can be observed, while the flow exhibits tall and thin structures under the effect of the strong global rotation, with a wide range of excited scales. We also observe torsional waves, which appear to be forced near the tangent cylinder. Using intensive post-processing, we analyze the fields and forces as a function of time- and length-scale in the two dynamically distinct regions separated by the imaginary cylinder aligned with rotation axis and tangent to the inner-core.

The rest of this paper is organized as follow. In the next section, we describe our numerical model, as well as the simulation targets. Then we describe and analyze our set of simulations, focusing on both averaged fields and rapid dynamics. We conclude the paper with a discussion.

2 Model equations, target, and numerical methods

2.1 Model

In order to simulate the liquid core of the Earth, confined between the solid inner core and mantle, we consider a spherical shell with an inner boundary at radius $r = r_i$ and an outer boundary at $r = r_o$. The aspect ratio is fixed to $r_i/r_o = 0.35$, as for the present Earth. The solid boundaries are at rest in the reference frame rotating at a constant rate Ω along the z-axis. The fluid has an electrical conductivity σ and a kinematic viscosity ν, both being constants (in space and time). Its magnetic permeability μ_0 is that of empty space.

The widely used Boussinesq approximation, coupled with the induction equation via the Lorentz force, is solved numerically from an initial condition. We use the codensity formulation (Braginsky and Roberts, 1995), which mixes buoyancy effects due to temperature variations and chemical species concentration into one scalar codensity field C, with associated diffusivity κ. The acceleration of gravity is in the radial direction and proportional to the radius r. At the outer boundary ($r = r_o$) the radial gravity is g and the codensity gradient is $\beta = -\partial_r C|_{r_o}$. We choose as length-scale the shell thickness $D = r_o - r_i$, and as time-scale the viscous time-scale D^2/ν. The resulting non-dimensional equations that will be time-stepped numerically read:

$$\partial_t \mathbf{u} + \left(\frac{2}{E}\,\mathbf{e_z} + \nabla \times \mathbf{u} \right) \times \mathbf{u} = -\nabla p + \Delta \mathbf{u} + (\nabla \times \mathbf{b}) \times \mathbf{b} - \frac{Ra}{\beta_0}\, C\, \vec{r} \tag{1}$$

$$\partial_t \mathbf{b} = \nabla \times (\mathbf{u} \times \mathbf{b}) + \frac{1}{Pm} \Delta \mathbf{b} \tag{2}$$

$$\partial_t C + \mathbf{u}.\nabla(C + C_0) = \frac{1}{Pr} \Delta C \tag{3}$$

$$\nabla.\mathbf{u} = 0 \qquad\qquad \nabla.\mathbf{b} = 0 \tag{4}$$

with the Ekman number $E = \nu/D^2\Omega$, the Rayleigh number $Ra = \beta g D^4/\kappa\nu$, the magnetic Prandtl number $Pm = \nu\mu_0\sigma$, and the Prandtl number fixed to $Pr = \nu/\kappa = 1$. $\mathbf{u}$ is the velocity field and $\mathbf{b}$ the magnetic field in (Alfvén) velocity units (i.e. it has been scaled by $\sqrt{\mu_0\rho}$, where ρ is the homogeneous core density).

The conductive codensity profile $C_0(r)$ is obtained using the thermochemical model of Aubert et al. (2009), with a fraction $f_i = 0.75$ of buoyancy due to light element release at the inner-core boundary:

$$C_0(r) = c_i \frac{r^2}{2} + c_o \frac{1}{r}, \tag{5}$$

with

$$c_i = \frac{(2f_i - 1)}{r_o^3 - r_i^3} \simeq 0.143, \qquad c_o = \frac{f_i r_o^3 - (1 - f_i) r_i^3}{r_o^3 - r_i^3} \simeq 0.772. \tag{6}$$

This profile has a gradient at the outer boundary $\beta_0 = -\partial_r C_0|_{r_o} = -c_i r_o + c_o/r^2 \simeq 0.1056$.

At both inner and outer boundaries, the codensity gradient $\partial_r C$ is fixed to zero (corresponding to a constant uniform heat flux), the velocity is zero (no-slip), and the magnetic field is matched to a potential field outside the fluid domain (the inner-core and mantle are both electrically insulating).

2.2 Target features for our simulations

The Earth's core operates at low viscosity (as measured by $E \simeq 10^{-15}$ and $Pm \simeq 10^{-6}$), so we should try to lower E and Pm as much as possible. Figure 1 (left) illustrates the difficulty to lower E and Pm: the magnetic Reynolds number Rm (represented by the size of the circles) decreases and at some point it is not enough to maintain a magnetic field against ohmic dissipation.

Another outstanding feature of Earth's dynamo is the small ratio of kinetic to magnetic energy, which is the squared Alfvén number $A^2 \simeq 10^{-4}$. It is apparent in Figure 1 (right) that low A are difficult to obtain for $Pm < 1$. Low Alfvén number dynamos are readily obtained with $Pm \geq 1$ (e.g. Kageyama et al., 2008; Dormy, 2016) and just above the convection threshold (e.g. Takahashi and Shimizu, 2012). Imposing the heat flux rather than the temperature at the boundaries also helps to get a strong magnetic field (Sakuraba and Roberts, 2009), although this may be linked to the fact that with fixed flux the convective power is proportional to Ra, whereas for fixed temperature the convective power is proportional to $(Nu - 1)Ra$, leading to weaker driving power in the fixed flux case for the same value of super-criticality Ra/Ra_c (Aubert et al., 2017, Fig. 1).

Our goal is to obtain vigorous convection (far above its onset) and low Pm dynamo with a strong magnetic field ($A < 1$).

When trying to compute geodynamo models as close as possible to the parameters of the Earth's core, the computation cost increases not only because of the higher and higher spatial resolution required, but also because the time-step is smaller and smaller compared to the magnetic diffusion time. Hence, in order to reach a statistically stationary dynamo

regime, the time needed for a simulation to run increases prohibitively [1]. To reach extreme parameters in our simulations, we prepare the initial conditions close to the expected statistical equilibrium state, in order to reduce the duration of transients. Those initial conditions are obtained by applying previously established scaling laws (Christensen and Aubert, 2006) to the output of a lower resolution simulation at parameter further from the Earth's core. This procedure can be repeated to achieve simulations that are closer and closer to the conditions of the Earth's core.

2.3 Numerical implementation

We use the XSHELLS code, available as free software[2]. It passes the dynamo benchmark of Christensen et al. (2001) as reported by Matsui et al. (2016). It uses second order finite differences in radius and pseudo-spectral spherical harmonic expansion. The time-stepping scheme is second order in time, and treats the diffusive terms implicitly, while the non-linear and Coriolis terms are handled explicitly. We have carefully optimized The code for speed. The SHTns library (Schaeffer, 2013) performs all the spherical harmonic transforms and, thanks to its low memory requirement and high performance, we can reach high resolutions (up to harmonic degree $L_{max} = 1000$ in this study). A domain decomposition in the radial direction allows efficient parallel execution using multiple processes (using the MPI standard). In addition, within each process, multiple threads (using the OpenMP standard) are used for an added level of parallelism. The most demanding simulation presented below has been run routinely up to 8192 cores with a good scaling of the run time with the number of cores. More details about performance can be found in Matsui et al. (2016) and in the user manual[2].

3 The simulations

3.1 Overview

We have run three dynamo simulations (S0, S1, S2) that have decreasing Ekman numbers, $E = 10^{-5}$, 10^{-6} and 10^{-7} respectively. They all have a magnetic Reynolds number Rm between 500 and 700. This is achieved by lowering the magnetic Prandtl number Pm and increasing the Rayleigh number to preserve high supercriticality ($Ra/Ra_c > 7500$ is almost constant, where Ra_c is the Rayleigh number for the onset of non-magnetic convection). In order to avoid transients, initial fields for simulations S1 and S2 are produced from S0 and S1 respectively, by multiplying each field by a scaling factor to reach the energy levels expected from the scaling laws of Christensen and Aubert (2006). Note that the S0 simulation is a continuation of the simulation presented by Fournier et al. (2012), and that parts of both S0 and S1 were used by Bouligand et al. (2016) with the same name.

[1] for our series of simulations, the computing resources needed to span a magnetic diffusion time increase by a factor of about 30 to 100 when the Ekman number is divided by 10

[2] `https://www.bitbucket.org/nschaeff/xshells/`

	K08	*S09*	*Y16*	*A17*	**S0**	**S1**	**S2**	Earth
N_r	511	160	181	624	256	512	1024	
N_θ	1024	384	640	200	448	720	1344	
N_ϕ	2048	768	1280	400	720	1440	2688	
time	0.016		0.05	0.12	2.2	0.51	0.052	
E	$9.4\,10^{-7}$	$2.4\,10^{-6}$	10^{-6}	10^{-8}	10^{-5}	10^{-6}	10^{-7}	$3\,10^{-15}$
Ra/Ra_c	~ 300	200	400*		7505	8875	9717	10^6 ?
Pm	1	0.2	0.4	0.045	**0.4**	**0.2**	**0.1**	$2\,10^{-6}$
Pr	1	1	1	1	1	1	1	0.1 - 10
Rm	700	120	346	1082	**671**	**546**	**570**	2000
A	0.42	0.65	0.3	0.11	**1.2**	**0.43**	**0.36**	0.01
Re	700	600	865	24000	1680	2730	5700	10^9
Ro	$7.6\,10^{-4}$	$1.4\,10^{-3}$	$8.7\,10^{-4}$	$2.4\,10^{-4}$	0.017	$2.7\,10^{-3}$	$5.7\,10^{-4}$	$3\,10^{-6}$
Le	$1.8\,10^{-3}$	$2.2\,10^{-3}$	$2.9\,10^{-3}$	$2.1\,10^{-3}$	0.014	$6.4\,10^{-3}$	$1.6\,10^{-3}$	10^{-4}
Λ	3	0.4	3.4	20	8.0	8.2	2.5	1 - 10 ?

Table 1: Various input and output parameters of our dynamo simulations (S0, S1 and S2) compared to the Earth's core and the simulation of Kageyama et al. (2008) labeled *K08*, the UHFM case of Sakuraba and Roberts (2009) labeled *S09*, and the least viscous cases of Yadav et al. (2016b) and Aubert et al. (2017) labeled *Y16* and *A17* respectively. We use the following definitions: $E = \nu/D^2\Omega$, $Pm = \nu\mu_0\sigma$, $Pr = \nu/\kappa$, $Rm = UD\mu_0\sigma$, $A = \sqrt{\mu_0\rho}U/B$, $Re = UD/\nu$, $Ro = U/D\Omega$, $Le = B/\sqrt{\mu_0\rho}D\Omega$, $\Lambda = B^2\sigma/\rho\Omega$. The numbers of *K08*, *S09*, *Y16* and *A17* have been cast to our definitions, where D is the shell thickness, U the rms velocity and B the rms magnetic field averaged over the whole fluid domain. The number of discretization points in the radial, latitudinal and longitudinal directions are denoted by N_r, N_θ and N_ϕ respectively. The *time* refers to the simulated time, normalized by the magnetic diffusion time $D^2\mu_0\sigma$. Ra/Ra_c is the Rayleigh number divided by its value Ra_c at the onset of convection for the same Pr and E. For S0, S1 and S2, Ra_c has been computed precisely using the SINGE eigenmode solver (Vidal and Schaeffer, 2015). * Note that Ra/Ra_c for *Y16* has been multiplied by their Nusselt number to account for the different thermal boundary conditions (fixed temperature for *Y*16).

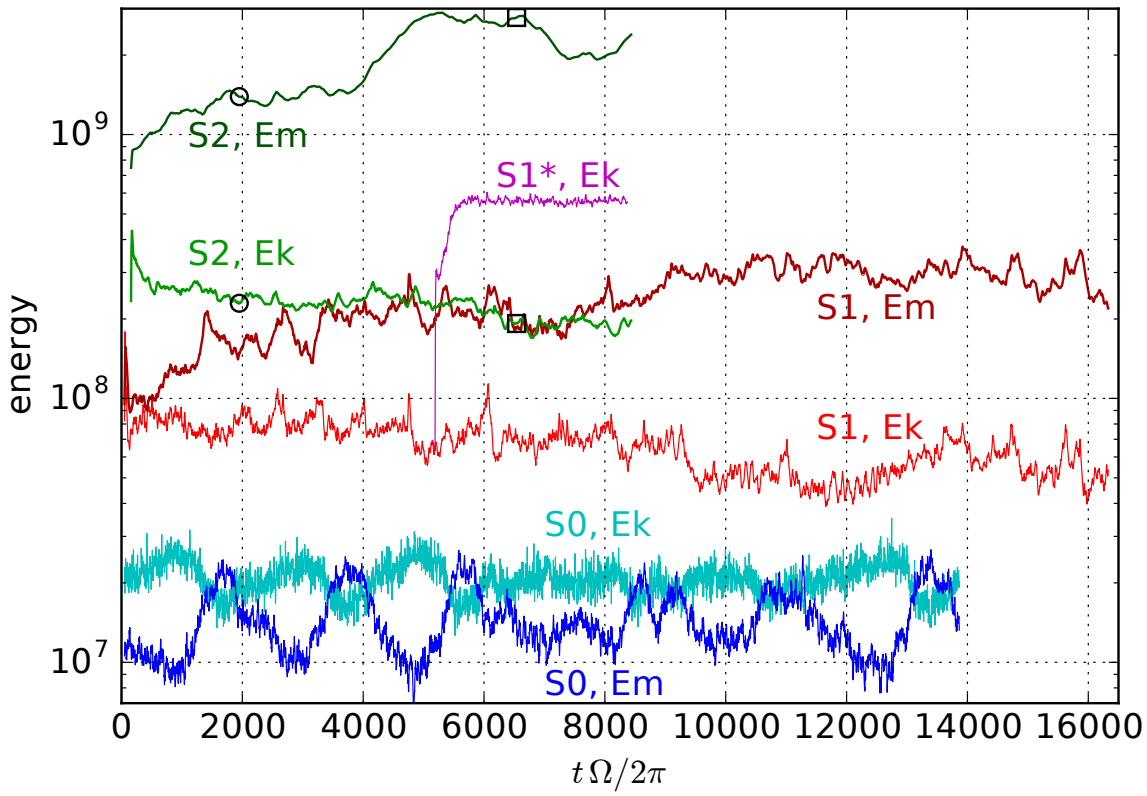

Figure 2: Kinetic (Ek) and magnetic (Em) energies as a function of time (normalized by the rotation period $2\pi/\Omega$) for our four cases (S0, S1, S1* and S2). For S1 and S2, magnetic energy is much larger than kinetic energy. The circles and squares mark the instants that are displayed in section 3.3.

In order to quantify the influence of the magnetic field, we have run a fourth simulation, S1*, which has the same parameters as S1, but without magnetic field. S1* is started from velocity and codensity fields of S1 at a given time, without any rescaling.

Table 1 summarizes the input parameters of our simulations, and compares it to the simulations of Kageyama et al. (2008), Sakuraba and Roberts (2009), Yadav et al. (2016b) and Aubert et al. (2017). The table also includes some output parameters computed from averaged quantities. No magnetic polarity reversal occurred in our simulations.

Figure 2 shows both kinetic and magnetic energies as a function of time, for our four simulations. It is clear that the ratio of magnetic over kinetic energy increases significantly from S0 to S2. In addition, the kinetic energy of S1* is about 10 times larger than that of S1, showing the strong influence of the magnetic field. In S1 and S2, the magnetic energy has fluctuations of larger amplitudes but lower frequencies than the kinetic energy. Furthermore, all the dynamo simulations exhibit much larger variations of their energy levels compared to the non-magnetic case S1*. This seems to be an inherent property of turbulent dynamo simulations. We note that the magnetic energy in S1 and S2 increases above the level expected by the scaling laws of Christensen and Aubert (2006). However, considering the variability of the magnetic energy in S0, we cannot further test the validity of the scaling laws.

We have checked the spatial convergence of S2 by multiplying the number of radial shells by 1.5, and the maximum degree of spherical harmonics by 1.12. No noticeable difference was found in the energy levels. Furthermore, the highest degrees of the spherical harmonic spectra are always and for every radius about two orders of magnitude below the most energetic degree at that radius.

3.2 Mean fields

Time and longitude averaged fields are represented in figure 3, for the three dynamo simulations S0, S1 and S2, and for the non-magnetic convection simulation S1*.

The root-mean-square (rms) poloidal magnetic field is comparable to the toroidal one, with a poloidal over toroidal ratio of 1.73, 0.95 and 0.83 for simulations S0 to S2. In all three cases, the amplitude of meridional velocity is weak, about 4 to 6 % of the the zonal one.

A North-South asymmetry remains in S0 and S2 after averaging over the time when the required data is available (in terms of turn-over time: $T_{avg}/\tau_u = 1390$ for S0, 190 for S1, and 8 for S2). Note that a similar asymmetry is present in snapshots of S1 (not shown).

The imaginary cylinder tangent to the inner-core and aligned with the rotation axis (hereafter named tangent cylinder or TC) separates two regions of different dynamics. The lower the Ekman number, the sharper the transition between these two regions. This dichotomy is visible on both velocity components as well as on the toroidal magnetic field, for S1 ($E = 10^{-6}$) and S2 ($E = 10^{-7}$). A sharp shear layer, associated with a meridional circulation materializes the tangent cylinder, and is reminiscent of Stewartson layers (Stewartson, 1966). The zonal mean flow inside the tangent cylinder has amplitudes about 10 times larger than outside. This contrasts with the findings of Aubert (2005)

	S0	**S1**	**S1***	**S2**
E	10^{-5}	10^{-6}	10^{-6}	10^{-7}
Ra	$6.34\,10^{9}$	$1.27\,10^{11}$	$1.27\,10^{11}$	$2.54\,10^{12}$
Ra/Ra_c	7505	8875	8875	9717
Pm	0.4	0.2	0	0.1
Rm	671	546	0	514
A	1.2	0.43		0.27
Re	1680	2730	8760	5140
Ro	0.017	$2.7\,10^{-3}$	$8.8\,10^{-3}$	$5.1\,10^{-4}$
Le	0.014	$6.4\,10^{-3}$	0	$1.9\,10^{-3}$
Λ	8.0	8.2	0	3.7
Nu	31	45	42	59
f_{ohm}	59%	84%	0%	88%
L_u	0.020	0.011	0.014	$5.2\,10^{-3}$
L_b	0.022	0.025		0.023
$Ek(m=0)/Ek$	0.09	0.12	0.50	0.06
f_{dip}	0.49	0.72		0.67
$B_{surf}(l=1)/B_{rms}$	0.11	0.16		0.10
$\langle\|\mathcal{T}(s,t)\|\rangle_{s,t}$	0.447	0.161		0.119
$\langle\|\langle\mathcal{T}(s,t)\rangle_t\|\rangle_s$	0.257	0.0247		0.0219

Table 2: f_{ohm} is the fraction of ohmic dissipation. The Nusselt number Nu is computed by $(1+(C(r_o)-C(r_i))/(C_0(r_o)-C_0(r_i)))^{-1}$. $L_u = u_{rms}/\omega_{rms}$ and $L_b = b_{rms}/j_{rms}$ are velocity and magnetic field length-scales. Values given for S2 are obtained using time-averages over the last half of the time series (with strongest field). For definition of f_{dip} and $\mathcal{T}$ see section 3.4 and 3.9 respectively.

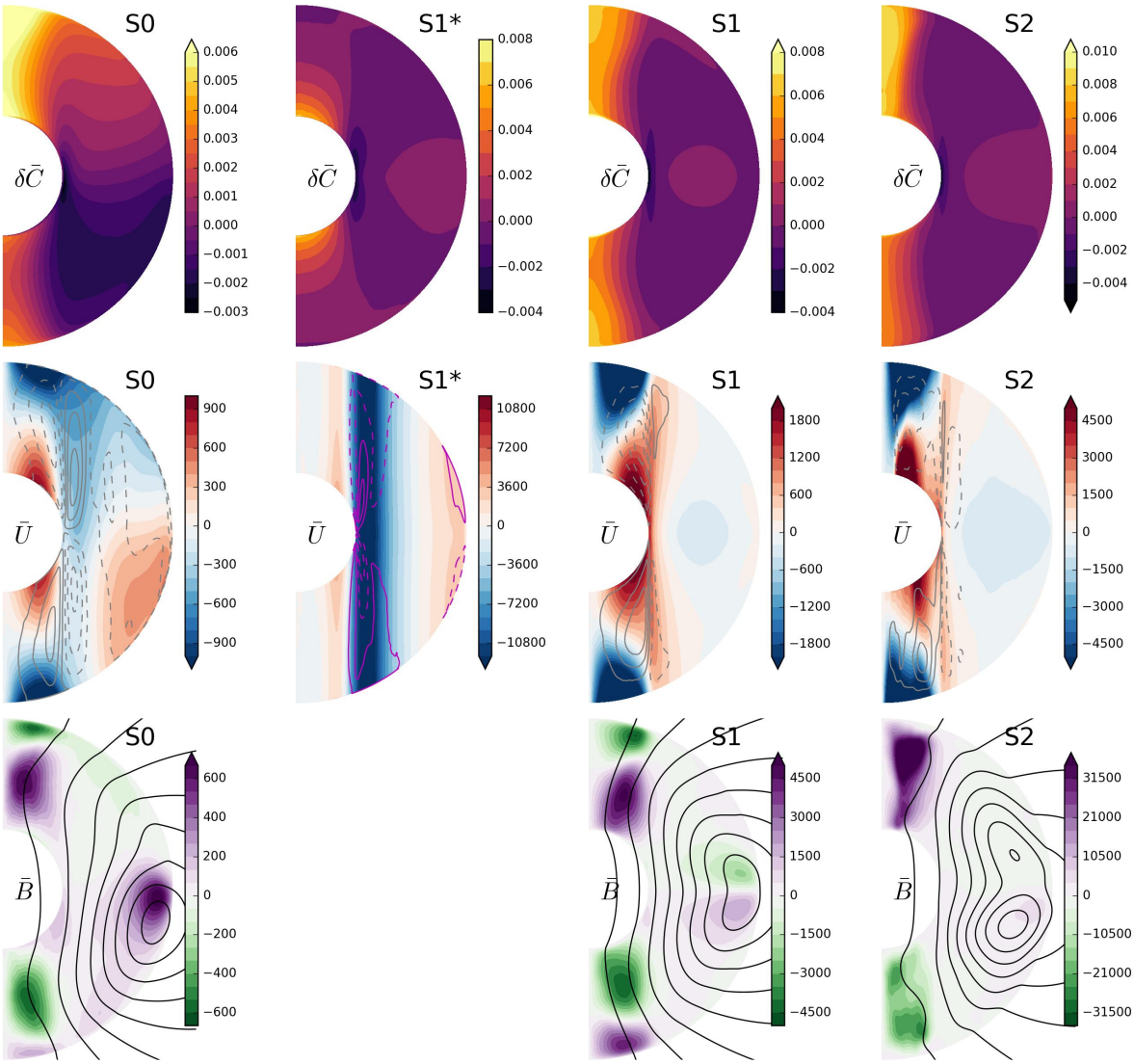

Figure 3: Time and longitude averaged codensity (top row), velocity (middle row) and magnetic (bottom row) fields in our simulations. For vector fields, the color map shows the azimuthal (toroidal) field (U_ϕ or B_ϕ), while the contours represent the meridional (poloidal) field lines. The magnetic energy contained in the poloidal field is about 0.9 the one contained in the toroidal field. The codensity fields are plotted after removing the mean radial profile. The parameters of simulations S0, S1, S1* and S2 are given in table 2.

who argued for iso-rotation along magnetic field lines and had comparable flow amplitudes inside and outside the tangent cylinder. However, we checked that the scaling of the zonal flow proposed by Aubert (2005) seems to hold.

Interestingly, the codensity perturbation (once the mean radial profile has been removed) shows that lighter fluid is trapped within the tangent cylinder (see also Fig 7). This feature is much less pronounced in the non-magnetic case S1*.

3.2.1 Outside the tangent cylinder

Outside the tangent cylinder, the averaged flow is weak in both S1 and S2. The zonal wind amplitude is $Ro \simeq 5 \times 10^{-5}$ in S2, about 10 times smaller than the overall rms averaged Rossby number (see table 2). In particular, the zonal wind is 10 times smaller than the one inside the tangent cylinder, and 30 times smaller in S1 than for the corresponding non-magnetic thermal convection of S1* (see figure 3), showing the strong effect of the magnetic field on the mean flow. Note also that the weak mean flow just below the equator of the core-mantle boundary (CMB) is rather eastward in S1 (positive), but westward in S2 (negative). The mean toroidal magnetic field is also weak in S1 (corresponding Elsasser number $\Lambda \simeq 0.05$) and even more so in S2 ($\Lambda \simeq 0.01$), but the poloidal field is rather strong, especially near the inner-core (where the associated Elsasser number reaches 0.25 in S2).

3.2.2 Inside the tangent cylinder

Inside the tangent cylinder, a strong azimuthal flow takes place, in the prograde direction close to the inner-core, and in the retrograde direction close to the mantle, with an associated meridional circulation (one cell). The zonal flow amplitude is $Ro \simeq 5 \times 10^{-4}$ in S2, similar to the overall rms averaged Rossby number (see table 2). They form what has been coined as polar vortices (Olson and Aurnou, 1999; Aubert, 2005). The anticyclonic polar vortex (near the CMB) has been associated with a low influence of inertia and a strong magnetic field (Sreenivasan and Jones, 2006). The structure of the flow resembles the Taylor vortices described in rotating thermal convection (e.g. Grooms et al., 2010), or a Von-Karman flow generated by two impellers co-rotating at different speeds (in order to obtain one meridional circulation cell). In this respect, the VKS experiment (Monchaux et al., 2009) may be not so far from the flow inside one hemisphere of the tangent cylinder. This contrasts with the non-magnetic case S1*, where the zonal flow is almost invariant along the rotation axis. Conversely, the codensity has little variations along the rotation axis in the dynamo simulations, but important ones in S1*. The twisted zonal flow within the tangent cylinder also reaches higher speeds in S1 than in S1*, suggesting that the strong toroidal field there allows the flow to break the Taylor-Proudman constraint imposed by the global rotation.

The toroidal magnetic field is concentrated here, suggesting that an omega effect is associated with the strong counter-rotating vortices (or twisted vortex) that dominate the mean flow. The Elsasser number associated with this strong toroidal field is close to unity

in S0, S1 and S2. At Elsasser close to one, convection onsets more easily and its length-scale increases dramatically from order $E^{1/3}$ to order 1 (Chandrasekhar, 1961; Aujogue et al., 2015). All conditions for such an effect are met within the tangent cylinder of S1 and S2. Note also that the toroidal magnetic field in S2 seems to have switched to another topology (only one sign in each hemisphere of S2 compared to the two regions of opposite sign in S1), with minor impact on the mean poloidal field (but see Fig. 8).

3.2.3 Non-zonal mean flows

Non-zonal mean flows appear to be a prominent feature of S2. Figure 4 shows velocity field averaged in time and along the rotation axis (z-axis – note that the average along z spans only one hemisphere within the tangent cylinder). In S1, the z-averaged mean flow is dominated by a prograde jet at the tangent cylinder and a retrograde circulation within. A weak large-scale non-zonal flow is still visible outside the TC in S1. When averaging over a shorter time-span (24 turn-over times instead of 190), the non-zonal flow dominates. The least viscous and strongly magnetized simulation S2 is dominated by a large non-zonal gyre outside the TC. Although arguably limited, the time span available for averaging the S2 flow is significant and would translate to about thousand years if the turn-over time is used for scaling to Earth values. Similarly, the non-zonal z-invariant flow seems to last about 24 turn-over times in S1, corresponding to more than 5000-10000 years. One outstanding difference between S1 and S2 is that the anti-cylclonic gyre leads to strong westward velocities at the equator in S2, whereas it is weak and mostly eastward in S1.

We emphasize that our setup and its boundary conditions have all a strict spherical symmetry (i.e. no heterogeneous thermal boundary conditions at the mantle or the inner-core). This shows that large scale circulations within the core (such as the excentric gyre identified from geomagnetic data, e.g. Pais and Jault, 2008; Pais et al., 2015; Gillet et al., 2015) can form spontaneously and last for a long time, as in S2, without the need for an heterogeneous thermal forcing at the mantle or the inner-core, not to mention a fine tuned gravitational coupling between mantle and inner-core (e.g. Aubert et al., 2013).

3.3 Instantaneous fields

We now turn to instant snapshots of the fields, which are represented in the equatorial plane for simulations S1 and S1* in Figure 5, contrasting the differences between dynamo (S1) and non-magnetic convection (S1*). The codensity field C exhibits very small scales near the inner-core where the plumes originate in both S1 and S1*. Further away from the inner-core, the codensity field exhibits much larger structures in S1 than in S1*. The plumes also reach further out in S1 whereas they seem to be stopped by the zonal winds in S1* (see U_r in Fig 5). However, the overall state is better mixed in S1* (lower contrasts in variations of C). This illustrates the effect of the magnetic field on the convection.

Figure 6 shows similar views for S2 at two different times characterized by moderate and strong magnetic fields (respectively marked by circle and square in Figure 2).

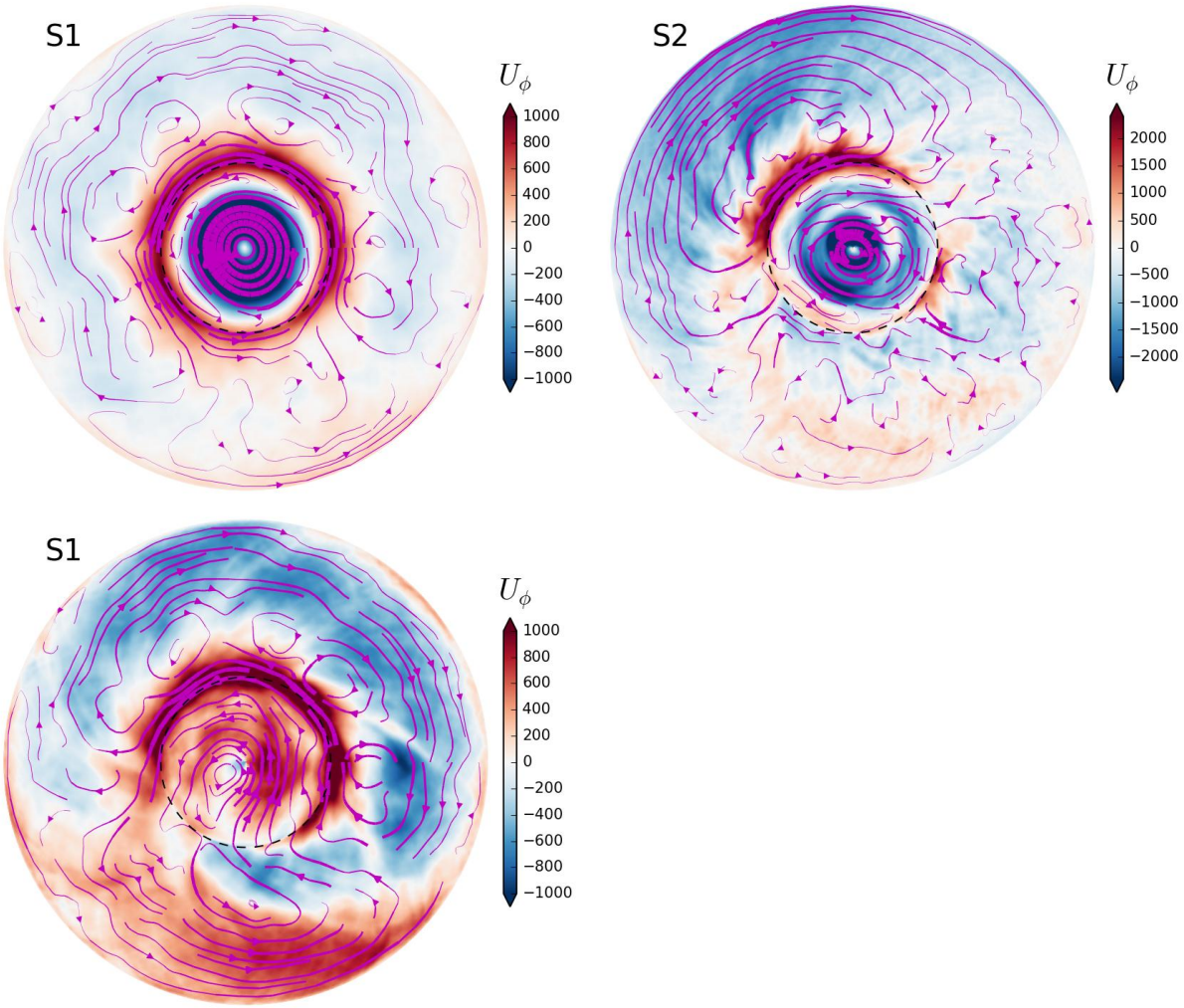

Figure 4: Mean flow (averaged in time and along the rotation axis) in simulations S1 (left) and S2 (right). The streamlines materializes the velocity field, while the color map highlights the azimuthal component. In these views from the north-pole, the black dashed circle indicates the location of the tangent cylinder. Top row: the time-average spans 0.35 magnetic diffusion time or 190 turn-over times for S1, and 0.016 magnetic diffusion time or 8 turn-over times for S2. Bottom row: the time-average spans 0.044 magnetic diffusion time or 24 turn-over times for S1.

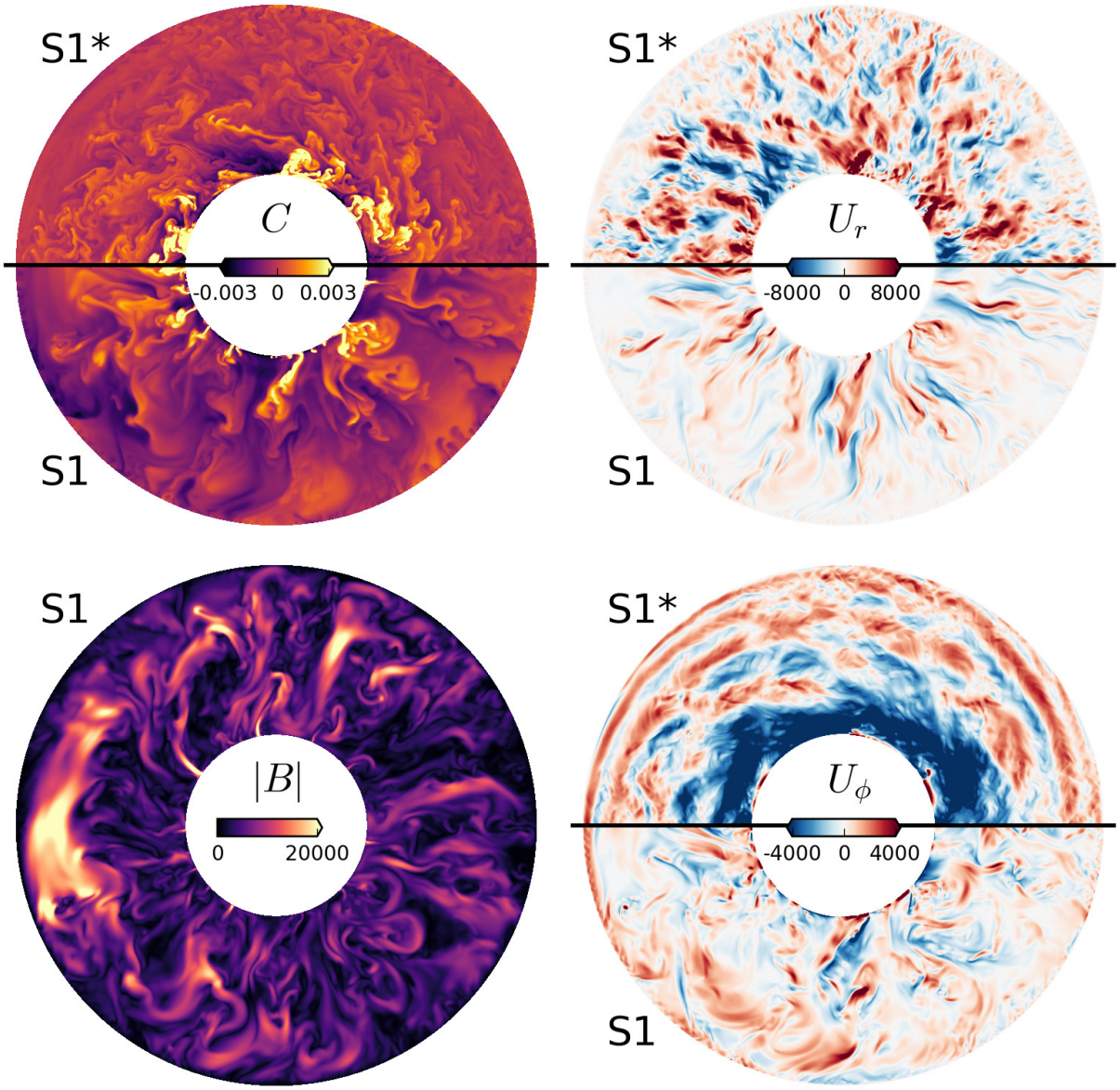

Figure 5: Snapshot of fields in the equatorial plane of simulation S1 ($E = 10^{-6}$, $Pm = 0.2$) and S1* ($E = 10^{-6}$, without magnetic field). The codensity (upper left panel) is represented after removing the mean value at each radius in the plane. The azimuthal velocity U_ϕ has been divided by 3 in S1* to fit the same color scale as S1. The snapshots are taken at the end of S1 and S1* simulations.

Three-dimensional renderings of the strongest field situation are shown in Figure 7. Very small-scale buoyant plumes originate near the inner-core for the moderate and strong field snapshots, but further away the scales appear larger where the strongest field reigns. Radial velocities are also weaker in these regions. There are noticeable velocity field patterns with azimuthal wavenumbers much smaller than $m = 70$ – the critical wavenumber at onset – especially in the strong field regions. These large scales coexist with smaller scales close to the inner-core, but also in regions of weaker magnetic field.

This enlargement of convection scale in a fixed flux simulation is in broad agreement with the observations made by Matsui et al. (2014) at higher Ekman numbers and lower forcing (see also Hori et al., 2012; Yadav et al., 2016b). The mechanism they propose does also fit our simulations. Namely, the presence of important variations of codensity over large regions (Fig. 6 top) produces non-axisymmetric thermal winds that convert the poloidal field into azimuthal field. The field inhibits motions, preventing the codensity anomalies to mix, thus sustaining the phenomena. Large scale motions induce less shear and are thus favored compared to small-scale convection.

We would like to emphasize that the large scale codensity anomalies can build up only because the zonal flow is suppressed by the magnetic field. Otherwise codensity anomalies are quickly mixed, as seen in the non-magnetic convection of S1* (Fig. 5).

In our simulations S1 and S2, magnetic field intensity is largely inhomogeneous (see $|B|$ in Figures 5, 6 and 7). This does not seem to affect the surface field which is already an order of magnitude smaller than the bulk average. Because the strength of the magnetic field is expected to control the length-scale of convection, then convection in planetary core would span a wide range of length-scales, possibly from the viscous scale $E^{1/3}$ to the planetary scale. It is important to take this into account when conceptualizing turbulence in planetary cores (e.g. Nataf and Schaeffer, 2015).

We remark also that because the kinetic energy spectra are not steep enough, using the length-scale diagnostic introduced by Christensen and Aubert (2006, and widely used afterwards) fails to capture accurately the change in length-scale, especially since the viscous length-scale may still be present in the system when the Rayleigh number is highly super-critical as in our case, in contrast to the work of Matsui et al. (2014). This failure may also explain why the viscous length-scale was found to play a role in previous dynamo studies (King and Buffett, 2013) despite apparently strong magnetic fields.

3.4 Magnetic field at the core surface

It is important to look at the magnetic field at the surface of the core, as it can be readily compared with the geomagnetic field. Following (Christensen and Aubert, 2006), the fraction of axial dipole in the observable spectrum (up to $\ell = 13$) is given by f_{dip} in table 2, and is in reasonable agreement with the one of the Earth ($f_{dip} \simeq 0.68$). Figure 8 shows the magnetic field at the surface of S1 and S2 at a given time (the same time as in fig. 5 and 7). Interestingly, the surface magnetic field displays similarities with the surface codensity (see Fig. 7), in particular sharp gradients near the tangent cylinder.

An important feature of the Earth's magnetic field is its secular variation, and in

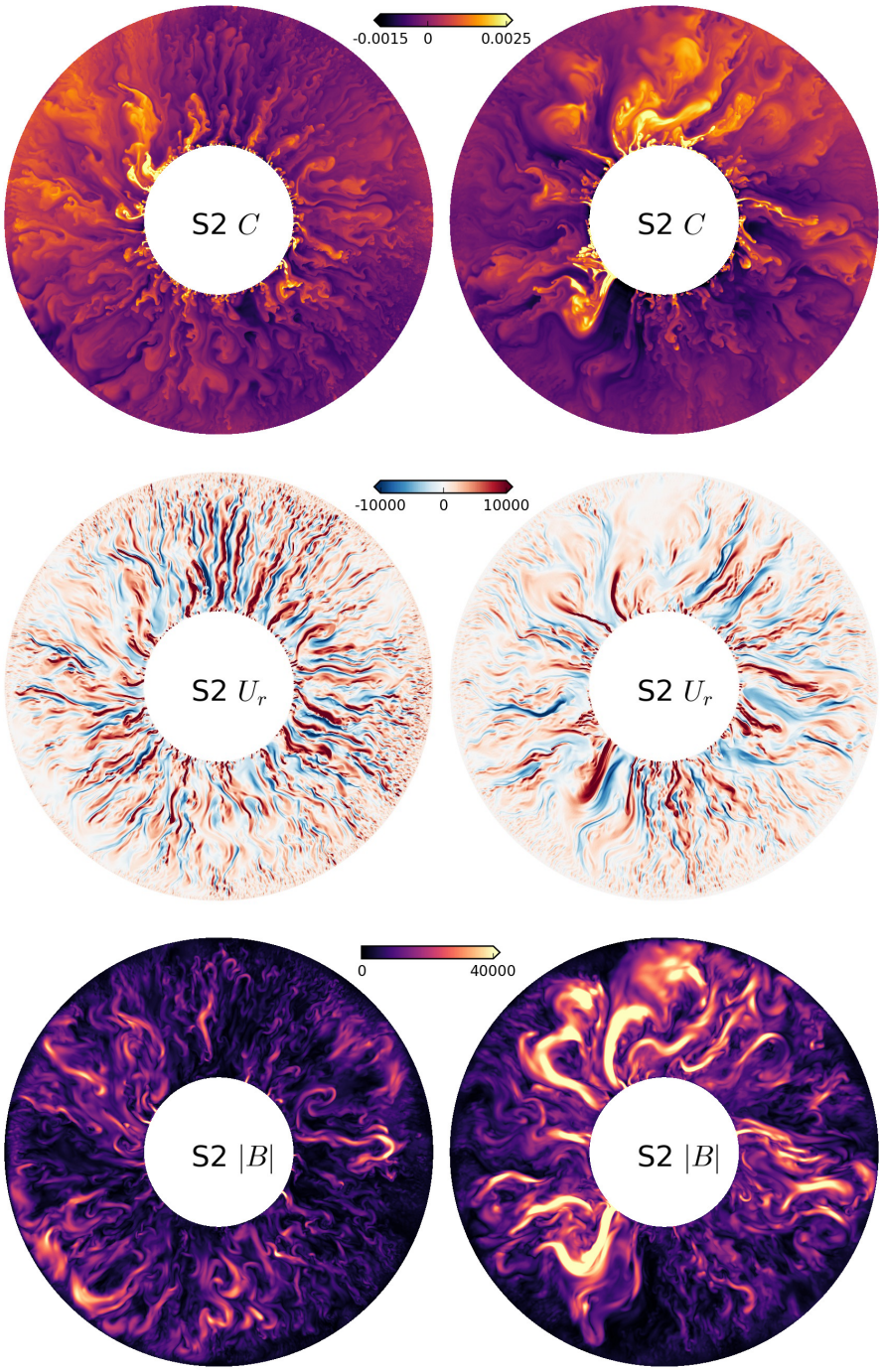

Figure 6: Snapshot of fields in the equatorial plane of simulation S2 ($E = 10^{-7}$, $Pm = 0.1$). Left: at a time with low magnetic energy (marked by a circle in Fig. 2). Right: high magnetic energy (marked by a square in Fig. 2). Top row: codensity (after removing the mean value at each radius in the plane). Middle row: radial component of the velocity field; Bottom row: intensity of the magnetic field.

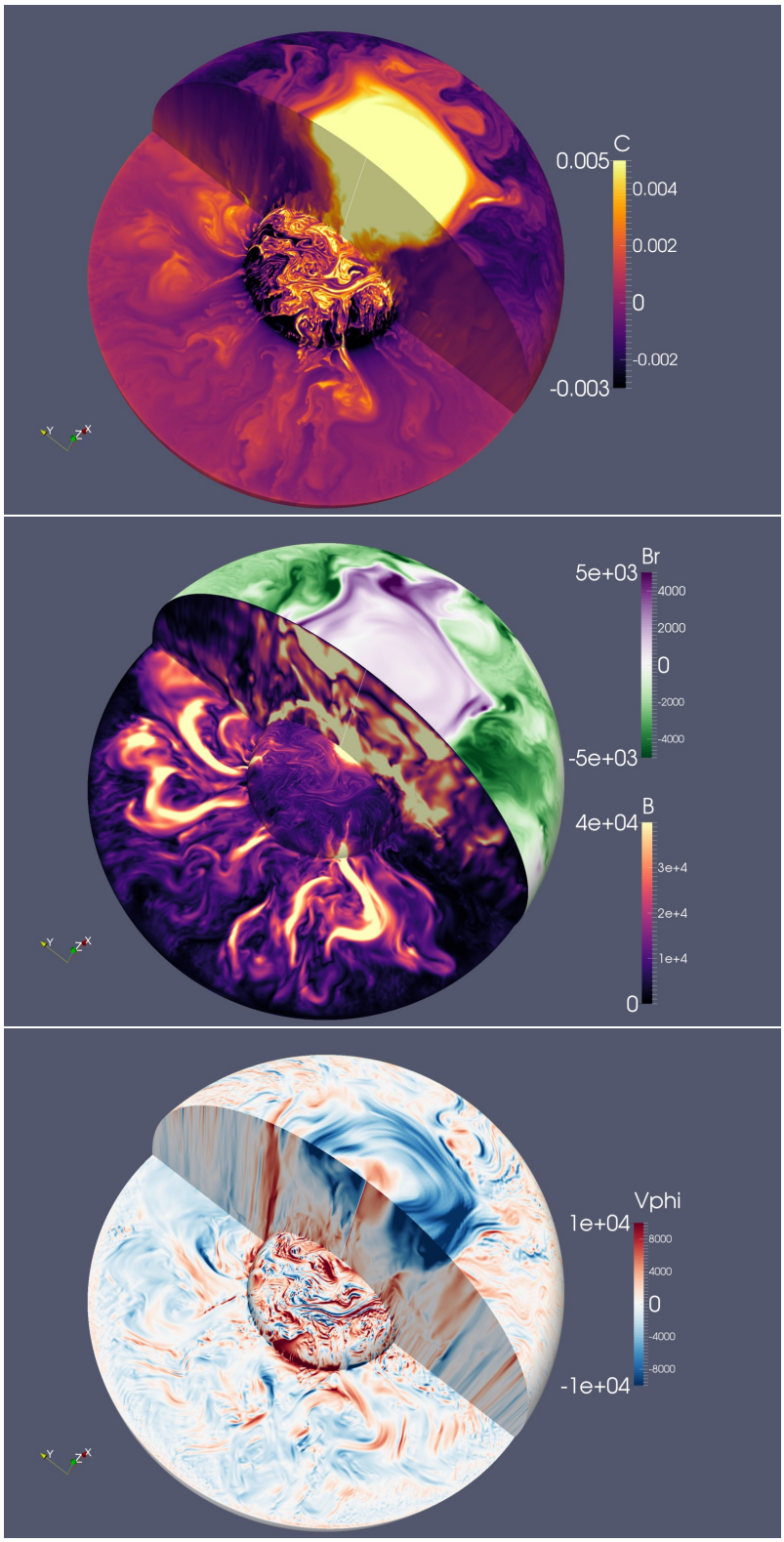

Figure 7: Three-dimensional renderings of the fields in the S2 simulation, at the instant marked by a square in figure 2. The white line is the rotation axis.

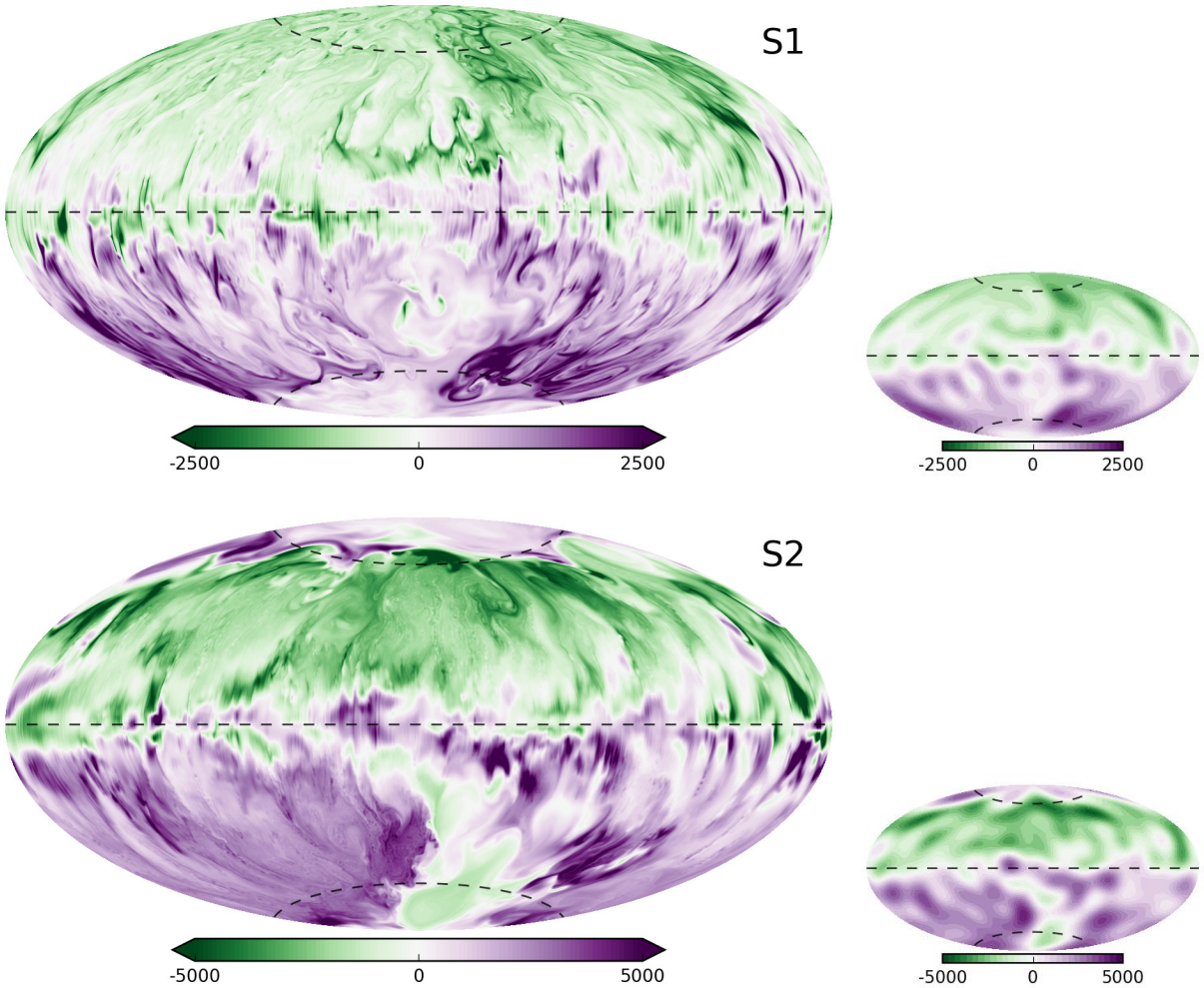

Figure 8: Aitoff projection of the radial magnetic field at the core surface in full resolution (left) and truncated after harmonic degree $\ell = 13$ (right). Top row: S1 ($E = 10^{-6}$, $Pm = 0.2$); Bottom row: S2 ($E = 10^{-7}$, $Pm = 0.1$). The dashed lines indicate the equator and the intersection with the tangent cylinder (latitude 69.5°).

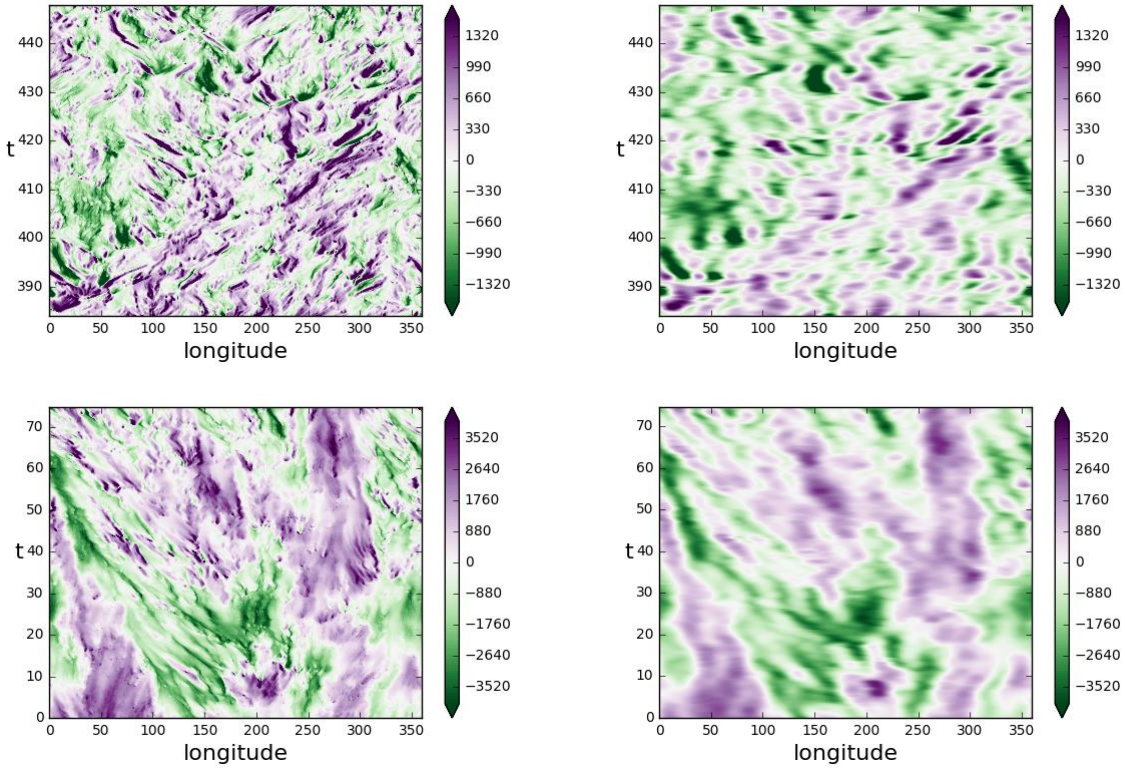

Figure 9: Time-longitude representation of the radial magnetic field along the equator. Top: simulation S1; bottom: simulation S2. Left: full field; right: truncated at $\ell = 13$. Time is in Alfvén time-scale units.

particular the westward drift of magnetic flux patches near the equator of the atlantic hemisphere. The evolution in time of the field at the equator is represented in figure 9 for S1 and S2. Whereas there is mostly eastward drift in S1, S2 displays an important region of westward drift (roughly between 30° and 180° longitude) together with a region with no net drift (around 300°). These plots also highlight the larger longitudinal extent of patches in S2 than in S1 and their longer life-span.

The westward drift in S2, restricted to one hemisphere, is consistent with the geomagnetic field data (e.g. Finlay and Jackson, 2003). The westward drifting region in S2 seen in figure 9 corresponds to the one with strong westward circulation in figure 4. This demonstrates that large-scale westward drift arises naturally in our less viscous simulation, in contrast with the model of Aubert et al. (2013), which requires heterogeneous heat flux at the boundaries together with a fine-tuned gravitational coupling between inner-core and mantle. In our simulation, the westward drift is due to the non-axisymmetric circulation seen in Fig. 4. We also notice the appearance of alternating polarity magnetic field with a well determined wave-length drifting west in the upper left part of the bottom left panel of Figure 9, akin to the equatorial slow waves of Finlay and Jackson (2003).

3.5 Fluctuations and Helicity

We compute the fluctuation maps shown in figure 10 by

$$U'(r,\theta) = \sqrt{\langle |U(r,\theta,\phi,t) - \bar{U}(r,\theta,\phi)|^2 \rangle} \tag{7}$$

where $\langle . \rangle$ denotes the average over longitude ϕ and time t. Similarly, the relative mean helicity H' from fluctuating field is computed with:

$$\mathbf{u}(r,\theta,\phi,t) = U(r,\theta,\phi,t) - \bar{U}(r,\theta,\phi) \tag{8}$$

$$\omega(r,\theta,\phi,t) = \nabla \times \mathbf{u} \tag{9}$$

$$H'(r,\theta) = \frac{\langle \mathbf{u}.\omega \rangle}{\sqrt{\int\int_{r,\theta} \langle \mathbf{u}^2 \rangle \ \int\int_{r,\theta} \langle \omega^2 \rangle}} \tag{10}$$

Velocity fluctuations are large in the polar regions just below the CMB and near the inner core boundary (ICB), but rather weak in between. This suggests that the velocity fluctuations inside the TC are associated to variability of the polar vortices. Outside the TC, velocity fluctuations are always small near the equator of the CMB, and increasing gradually towards the tangent cylinder, where the mean poloidal field is also concentrated.

To link these fluctuations with a possible poloidal magnetic field generation, we turn to helicity, which is often associated with alpha effect (e.g. Moffatt, 1978; Jones, 2008) whereby poloidal magnetic field is produced from toroidal field. Helicity fluctuations exhibit a gradual change. In S0 helicity is maximum near the boundaries and extends toward the equator just outside the TC. In S2 the maximum helicity in the outside region is located near the inner-core. S1 shows both boundary-layer bound helicity together with local

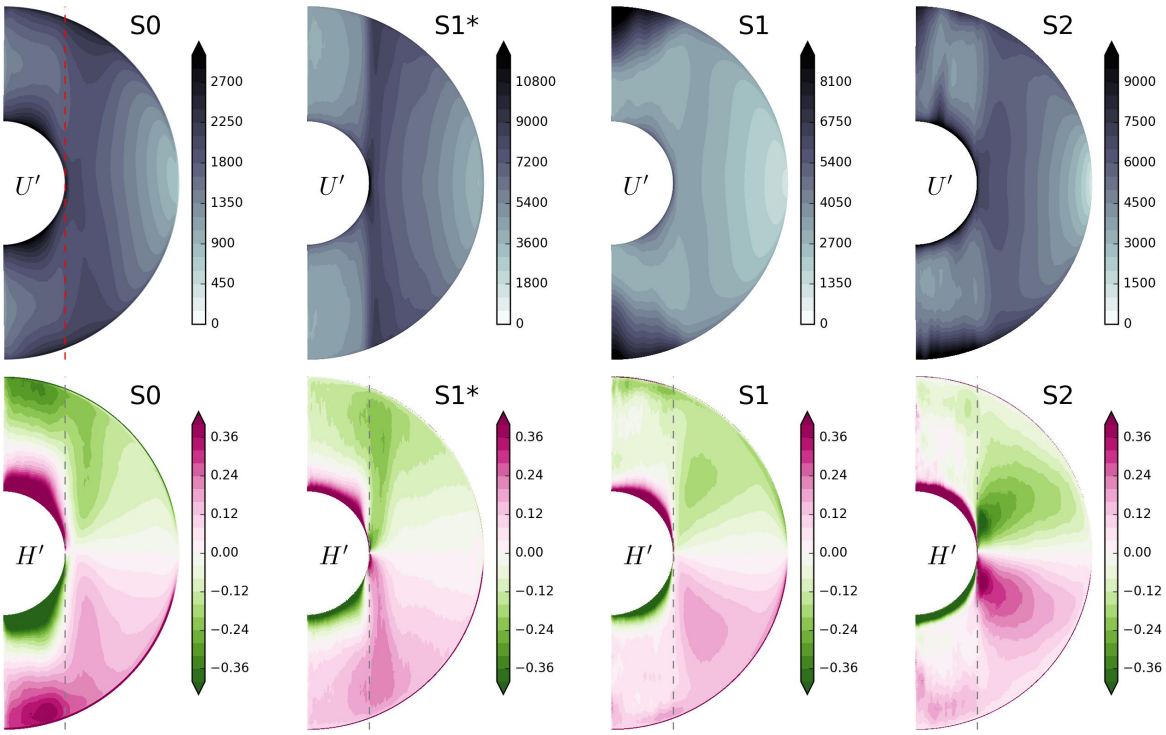

Figure 10: Time- and longitude-averaged fluctuating velocity (U') and relative helicity (H'). See text for definitions.

maximum in the bulk. Outside the tangent cylinder, relative helicity is larger in S2 than in S1 . This suggests a transition from Ekman pumping based helicity in S0 (see Busse, 1975), to bulk helicity in S2, which might be a hint for the mechanism proposed by Sreenivasan and Jones (2011, relying on magnetic pumping), or the one proposed by Davidson (2014, relying on inertial waves). In any case, we can confidently say that the S2 dynamo does not rely on helicity induced by Ekman pumping, as expected for the Earth's core (e.g. Schaeffer and Cardin, 2006).

3.6 Spectra

Figure 11 shows kinetic and magnetic energy spectra for all our simulations. These time- and radius- averaged spectra are misleading in several ways. First, they encompass regions with vastly different dynamics and length scale (inside and outside the tangent cylinder). Second, even in these regions, fluctuations are largely inhomogeneous (see Fig. 10). Finally, a given harmonic degree ℓ corresponds to different length-scale depending on the radius.

We remark however that the non-magnetic simulation S1* displays a significant range of kinetic energy spectrum obeying a $\ell^{-3/2}$ law. This contrasts with the kinetic energy spectra in the dynamo simulations S1 and S2, which are much less steep, being almost

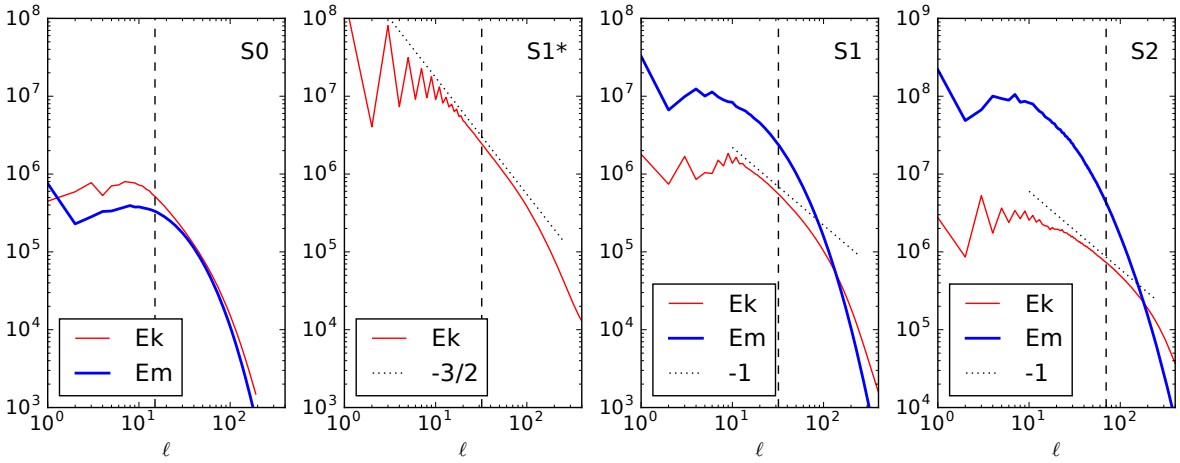

Figure 11: Time- and radius- averaged energy density spectra in our simulations, as a function of harmonic degree ℓ. The dashed vertical line marks the unstable wavenumber m_c at the onset of (non-magnetic) convection.

flat at large scales, and then displaying more or less a $\sim \ell^{-1}$ range. Christensen and Aubert (2006) introduced an *average harmonic degree* $\bar{\ell} = \sum_\ell \ell E_\ell(u) / \sum_\ell E_\ell(u)$. With a kinetic energy spectrum $E_\ell(u) \sim \ell^{-1}$, $\bar{\ell}$ will be determined by the smallest scales, although larger scales are present (see Fig. 4 and 11). This may explain why King and Buffett (2013) found that $\bar{\ell}$ seems to scale as the inverse of the viscous scale in a large database of dynamo simulations.

Figure 12 shows the energy spectra at 4 different radii in the S2 simulation. Near the inner-core ($r = 0.588$), the spectra are significantly influenced by the inside of the tangent cylinder. The strength of both velocity and magnetic fields at large scales ($\ell \leq 5$) is much larger than at larger radii.

In the middle of the shell ($r = 1.04$), the magnetic spectrum is not clearly dominated by the dipole component but is rather flat up to degree 20 to 30, and then decays quickly beyond $\ell \sim 50$. The kinetic energy spectrum is about 20 to 30 times smaller than the magnetic spectrum, and also peaks at degree $\ell \simeq 20$.

In the outer part ($r = 1.4$) the magnetic spectrum is not dominated by the dipole component $\ell = 1$, but peaks for degree $5 \leq \ell \leq 10$, just as the velocity spectrum.

We remark that at the surface ($r = 1.535$ – just below the Ekman layer), the magnetic spectrum is clearly dominated by the dipole. However, magnetic energy is much weaker than deeper in the shell. It is actually barely larger than the kinetic energy, unlike in the Earth. If we exclude the dipole ($\ell = 1$) and octupole ($\ell = 3$), the magnetic spectrum is rather flat up to degree $\ell = 10$. Beyond $\ell = 10$, both velocity and magnetic spectra decay slower than at lower radii.

Finally, note that the peaks in the spectra are always located at wavenumber signifi-

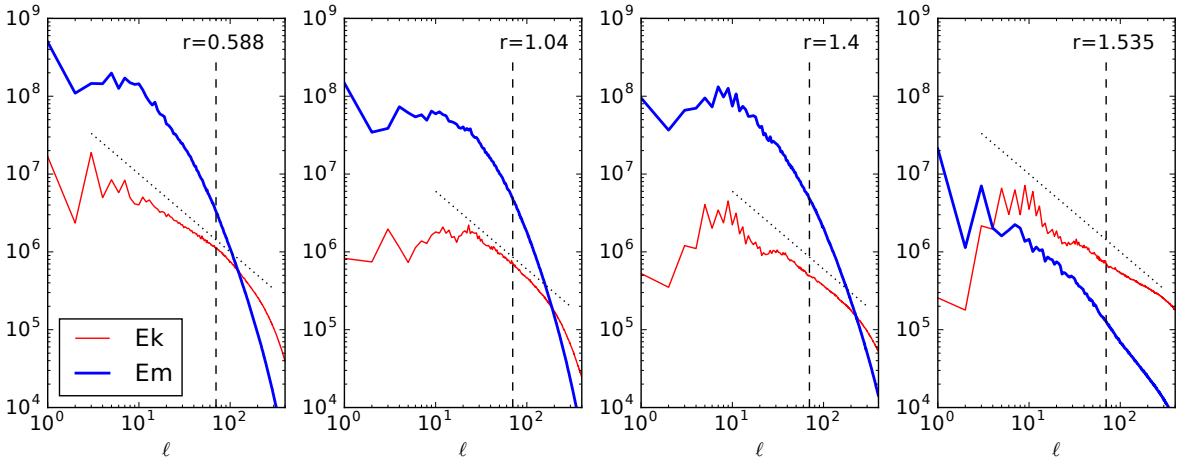

Figure 12: Time-averaged energy density spectra in simulation S2 at different radii. The dashed vertical line marks the unstable wavenumber $m_c = 70$ at the onset of (non-magnetic) convection. The dotted line is proportional to ℓ^{-1} to guide the eye.

cantly smaller than those expected at the onset of thermal convection ($m_{crit} = 70$).

3.7 Spatio-temporal Fourier analysis

Because of the vastly different dynamics occuring inside and outside the tangent cylinder, we need to analyze these regions separately. This cannot be done with simple harmonic degree spectra. Furthermore, the temporal fluctuations visible in Figure 2 also prompts us to analyze the fields and spectra beyond their time-averages.

We have recorded snapshots of the fields at regular time intervals. A full snapshot of S2 needs 32 gigabytes of disk space, and we could not afford to save many such large snapshots. For this reason, the many recorded snapshots are truncated at a spherical harmonic degree ℓ_{tr} that is smaller than the maximum ℓ_{max} resolved by the simulation: $\ell_{tr} < \ell_{max}$. To save even more disk space, we also use single-precision to store the snapshots. We apply a Fourier transform in time and longitude (the two homogeneous directions) to the whole snapshots series. Unfortunately, some snapshots have been lost. For S1, we could effectively use a series of 523 regularly spaced snapshots sampled at period $25/\Omega$ (every ~ 4 rotation periods or 8000 samples per magnetic diffusion time). For S2, only a series of 102 snapshots sampled at period $80/\Omega$ (every 12.7 rotation periods or 12500 samples per magnetic diffusion time). We then study separately five different regions, represented in Figure 13, inspired by the behavior of mean fields described above: an inner and outer boundary layer region, located near the inner-core and near the mantle respectively, with a radial extent of 10% of the outer shell radius; a tangent cylinder region, excluding the previous boundary layers and spanning cylindrical radii s from $0.3r_o$ to $0.4r_o$; an inner region for $s < 0.3$ and an outer

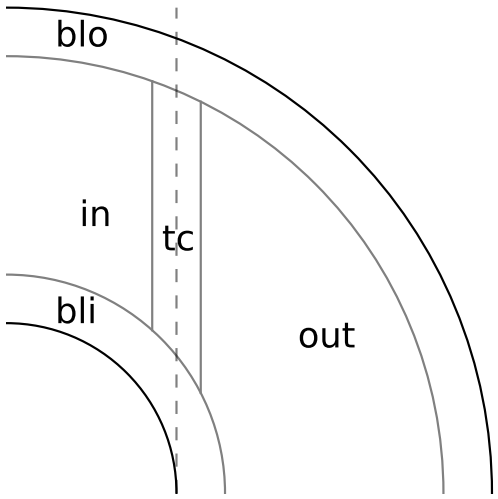

Figure 13: Meridional cut showing the five different axisymmetric regions of the simulation domain that are studied separately in the spatio-temporal Fourier analysis. *bli* and *blo* are boundary layer regions close to the inner-core and mantle respectively, of radial extent $0.1\,r_o$. *tc* is a region centered around the tangent cylinder spanning cylindrical radii $0.3 < s/r_o < 0.4$. *in* is a region located inside the tangent cylinder and excluding all other regions. *out* is the region outside the tangent cylinder, also excluding all other regions.

region for $s > 0.4$, both also excluding the two boundary layers. This allows us to describe quantitatively the temporal behavior of the fields in our simulations. For each snapshot, we also compute the different terms in the evolution equations and perform the same Fourier analysis, allowing to describe the dynamical balances in our simulations in terms of spatial and temporal scales (Nataf and Schaeffer, 2015).

3.7.1 Velocity and Magnetic fields

The critical azimuthal order for the onset of convection is $m_c = 15$, 32 and 70 for S0, S1 and S2 respectively. Figures 14 and 15 show that the azimuthal order of convection outside the tangent cylinder is around $m = 10$ for S1 and $m = 20$ for S2, which is significantly smaller than the scale for the onset of convection, although it is still dependent on the viscosity, scaling roughly as $E^{-1/3}$. However, in addition to this small scale convection, a non-zonal mean flow is produced in S2, and low frequency, low m flows are produced outside the tangent cylinder in S1 and S2. It is remarkable that in S2 the mean flow is dominated by $m = 1$ and 2 rather than $m = 0$. This mean flow is represented in Figure 4.

As already noticed, the dynamics is very different within the tangent cylinder. There, only large scale motion exists (the polar vortices), and the time-variability peaks at $m = 1$, meaning that this vortex keeps a rather constant amplitude but deviates from the global rotation axis. Axisymmetry ($m = 0$) dominates the magnetic field spectra.

The effect of the magnetic field can be seen by comparing figures 15 and 16. Without

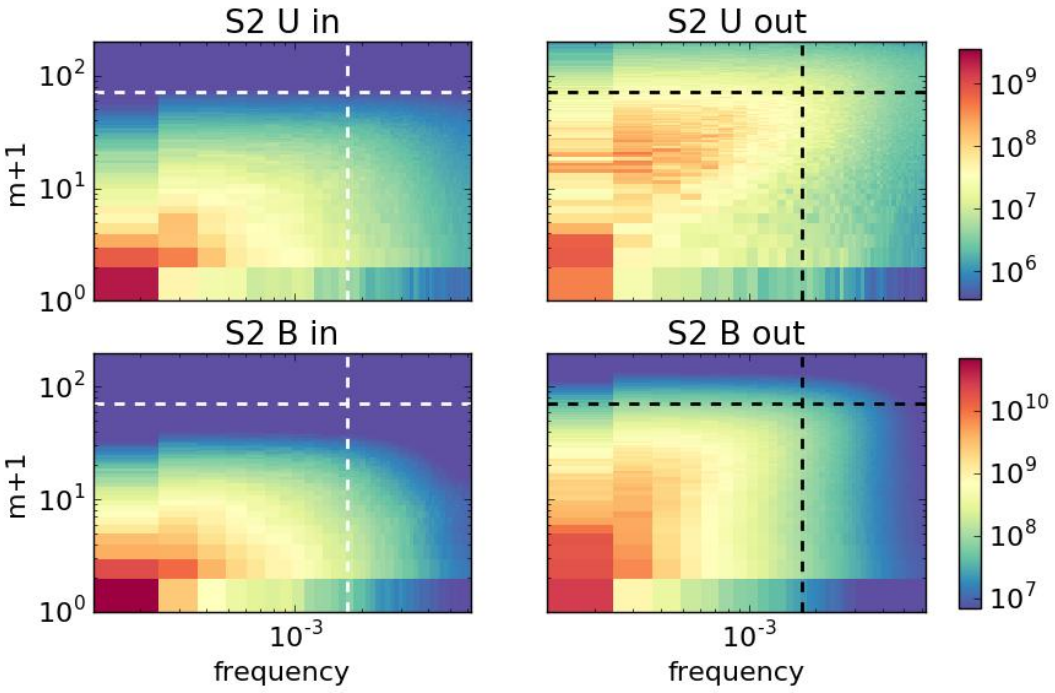

Figure 14: Space-time spectra of the kinetic (top) and magnetic (bottom) energies in S2, inside (left) and outside (right) the tangent cylinder (as defined in figure 13). The colormaps use a logarithmic scale, which is the same across regions allowing to compare or sum the energies of each region. Frequency is in units of rotation rate Ω, and has been shifted so that the leftmost column in each plot is the time-average (zero frequency). The dashed horizontal line marks the unstable mode at onset of convection, while the dashed vertical line marks the Alfvén frequency (Lehnert number).

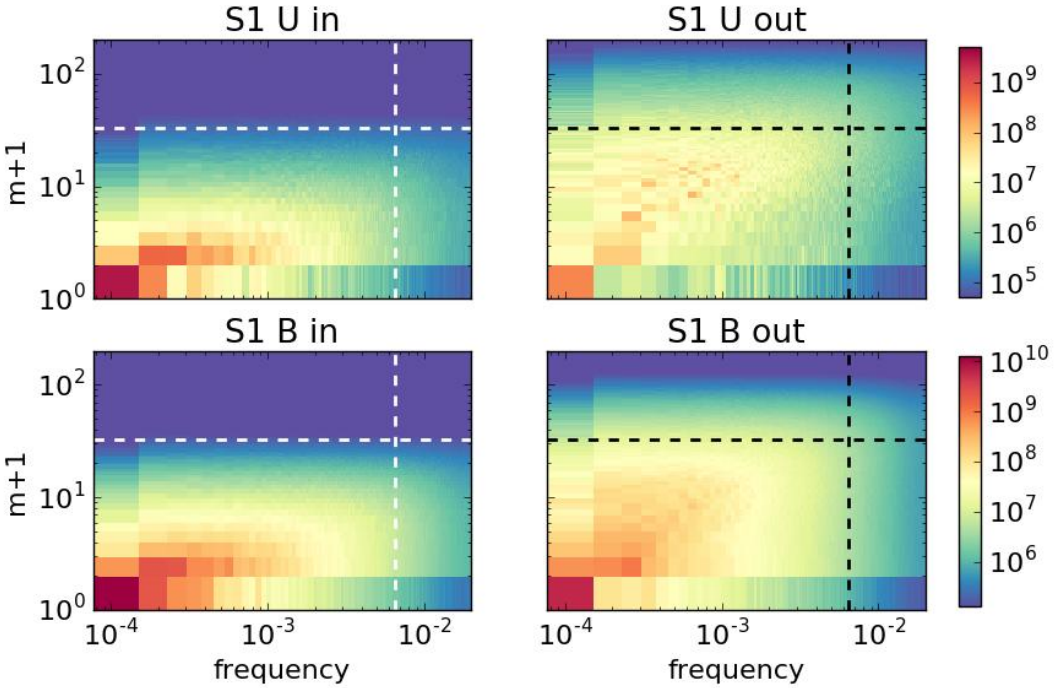

Figure 15: Space-time spectra of the kinetic and magnetic energies in S1. See caption of Fig. 14.

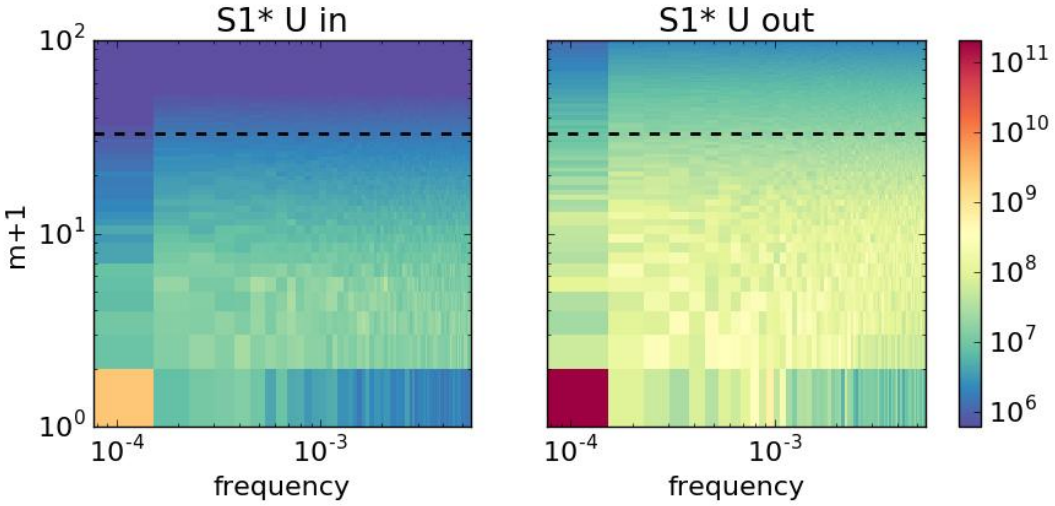

Figure 16: Space-time spectra of the kinetic energy in S1* (without magnetic field). See caption of Fig. 14.

magnetic field, the mean zonal flow dominates both inside and outside of the tangent cylinder, while more variability in both space and time is observed when the magnetic field is present, with important fluctuations of the $m = 1$ flow inside and outside the TC. Furthermore, the flow happens at all spatial and temporal scales, possibly fed also by instabilities of the zonal flow.

3.7.2 Dynamical balances

We apply a Fourier transform, in both azimuthal and time directions, to the different terms in the vorticity equation (the curl of equation 1). Note that examining the terms in the vorticity equation effectively extracts the second order balance, after the main geostrophic balance in which most of the Coriolis and pressure force have canceled each other. Fields were truncated to $\ell_{max} = 299$ before computing the terms, so we lose the contribution from the smallest scales to the non-linear terms. The spatial spectra shown in Figure 11 suggest that this is not a problem within the bulk, as the spectra start to decay well before $\ell = 100$, but we might loose significant contributions in the boundary layers. However, we have also checked that truncating further at $\ell_{max} = 100$ does not alter the broad picture.

The resulting two-dimensional spectra are represented in Figure 17 for each region and each term of simulation S2. Clearly, the different regions have very different dynamics, and averaging over all of them will definitely blur the analysis. Because the analyzed series spans only 1300 rotation periods for S2 (2081 for S1), we focus on the so-called rapid dynamics.

The broad picture, shown in Figure 17, consists of a clear dominance of Coriolis, Buoyancy and Lorentz terms in the interior regions (far from boundaries). This is consistent with the so-called MAC (Magneto-Archimedes-Coriolis) balance.

Close to the boundaries the balance involves mostly viscosity and Lorentz perturbed by the Coriolis term, which is compatible with the balance of a Hartmann layer. We notice that all forces are smaller for $m = 0$ than for $m > 0$, except for the time-average, which stands clearly out as a thermal wind balance, even outside the tangent cylinder. Remember however that the magnetic field plays a crucial role in establishing this particular flow. This analysis also illustrates the complexity of the spatio-temporal balances, which is completely overlooked when averaging in time. Note that for S1*, the balances do not depend on frequency (not shown).

With our spatio-temporal decomposition, we are able to refine the main MAC balance of the two interior regions. Figure 18 shows the relative importance of the Lorentz and Buoyancy terms. Specifically, the Coriolis term is mostly balanced by the Lorentz term in purple regions, and by the buoyancy term in orange regions.

Inside the tangent cylinder, the Lorentz term is somewhat sub-dominant at large scales, where a thermal wind balance describes well the largest scales and slow evolution. However, the Lorentz term does overcome the buoyancy at shorter time- and length-scales.

Outside the tangent cylinder, although the very weak mean flow is also controlled by a thermal wind balance, the Lorentz force is much more important. In fact, buoyancy plays a primary role at intermediate length-scales only (around $m = 20$). Note that this

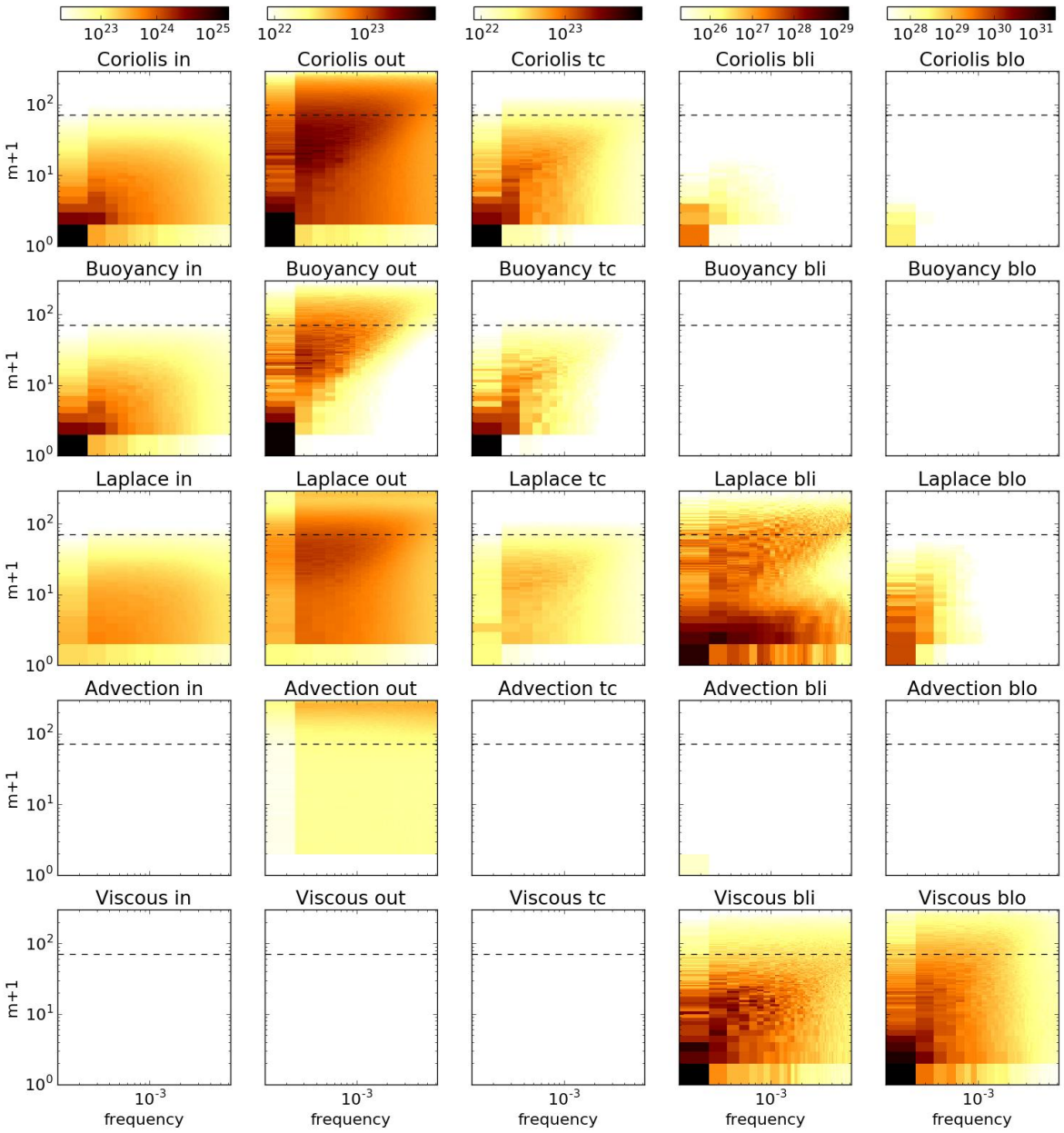

Figure 17: Space-time spectra of various terms in the vorticity equation of S2, in the regions defined in figure 13. The colormaps use a logarithmic scale. Advection is the curl of $u\nabla u$. Fields were truncated to $\ell_{max} = 299$ before computing each terms. The dashed horizontal line marks the unstable mode at onset of convection. Frequency is in units of rotation rate Ω, and has been shifted so that the leftmost tile in each plot is the time-average (zero frequency).

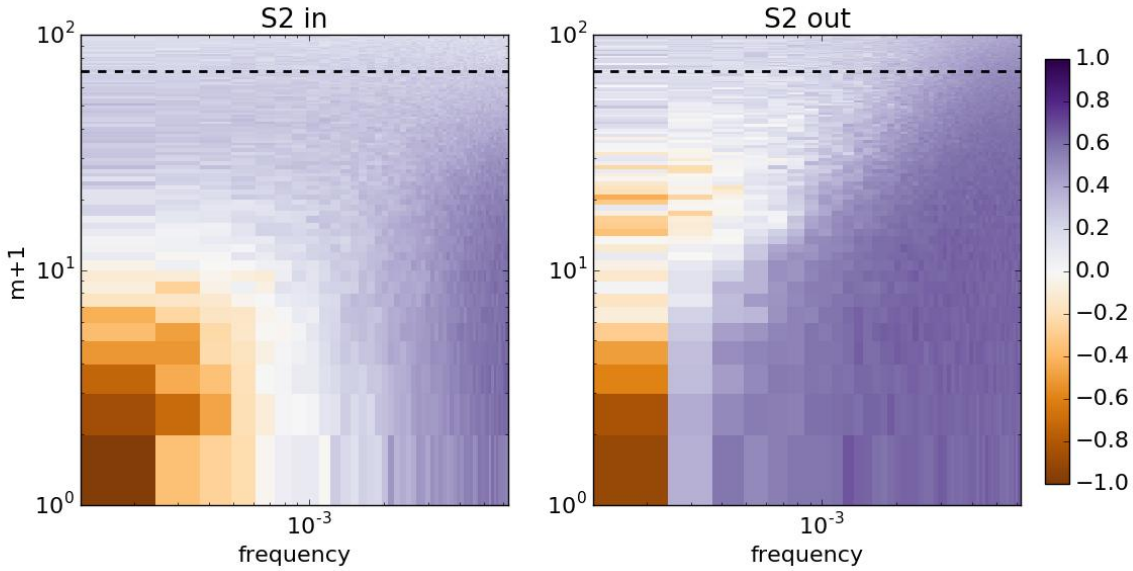

Figure 18: Deviations from MAC balance in the bulk of simulation S2 (bottom), as a function of azimuthal order m and frequency, inside (left) and outside (right) the tangent cylinder. The color maps show the quantity $(M-A)/C$ where M, A and C are respectively the rms of the Lorentz, Buoyancy and Coriolis terms in the vorticity equation. All values are between -1 and 1, except for the mean flow (lower left corner). The dashed horizontal line marks the unstable mode at onset of convection. Frequency is in units of Ω.

azimuthal wavenumber is much smaller than that of the onset of convection ($m_c = 70$). A magnetostrophic balance, involving mostly Coriolis and Lorentz terms, controls the rapid dynamics of the flow outside the tangent cylinder.

3.7.3 Flow invariance along the rotation axis

In order to quantify the z-invariance of the flow, we introduce

$$G_m(\omega, s_0, s_1) = \frac{\int_{s_0}^{s_1} \langle \mathbf{U}_m(\omega, s, z) \rangle_z^2 H(s)\, s\mathrm{d}s}{\int_{s_0}^{s_1} \langle \mathbf{U}_m^2(\omega, s, z) \rangle_z H(s)\, s\mathrm{d}s} \tag{11}$$

where $\langle \mathbf{U}_m(\omega, s, z) \rangle_z$ is the z-average of $\mathbf{U}_m(\omega, s, z)$, the order m Fourier transform coefficient along ϕ of the velocity field at frequency ω, at a given cylindrical radius s and distance above the equatorial plane z. $H(s)$ is the height of the cylinder of radius s embedded in the sphere. $G_m(s_0, s_1)$ is the energy of the z-averaged flow divided by the energy of the total flow, each computed between s_0 and s_1. $0 \leq G_m \leq 1$ is a measure of the geostrophy of the flow; for a geostrophic flow (i.e. independent of z), $G_m = 1$. Note also that a quasi-geostrophic flow, which has U_z depending (linearly) on z, will not have $G_m = 1$.

Figure 19 represents G_m within the tangent cylinder and outside the tangent cylinder. First we see that the large-scale flow in S1* have large values of G_m, indicating a high z-invariance of the flow, surprisingly even within the tangent cylinder. This invariance is lost at smaller scales, when the local Rossby number $Ro(m) = Ro\, m/\delta > 0.1$ – where $\delta = r_o$ for the outer region and r_i for the inner region. When influenced by a strong magnetic field, the z-invariance is completely lost inside the tangent cylinder, while it is only lowered outside, keeping a fair z-invariance, even more as the Lehnert number is decreased (compare results for S1 and S2, and see also Fig. 4), except for the axisymmetric mean flow. The quasi-geostrophic description (e.g. Schaeffer and Cardin, 2006; Gillet et al., 2011; Labbé et al., 2015) is thus relevant outside the tangent cylinder, even for time-scales which would correspond to several decades or even centuries (when rescaled using Alfvén or advective time-scales).

3.8 Torsional Alfvén waves

The high G values obtained for zonal flow at various frequencies together with a magnetic energy much larger than the kinetic energy suggest the presence of torsional waves. These Alfvén waves propagate in rapidly rotating systems with strong magnetic fields (see e.g. Jault and Finlay, 2015) and have been spotted in the Earth's core (Gillet et al., 2010, 2015). Figure 20 shows a space-time diagram of z-averaged zonal flow. Outside the tangent cylinder, the propagation of waves from the tangent cylinder ($s = 0.54$) towards the equator ($s = 1.54$) is striking. There are also a few events that propagate in the other direction, which seem to be spawned in the bulk. Similar waves are seen in S1, although the signal is a little bit more noisy (not shown). In S0, however, no such wave pattern appears. Interestingly, because the mean zonal flow is weak in our S1 and S2 simulations, we observe

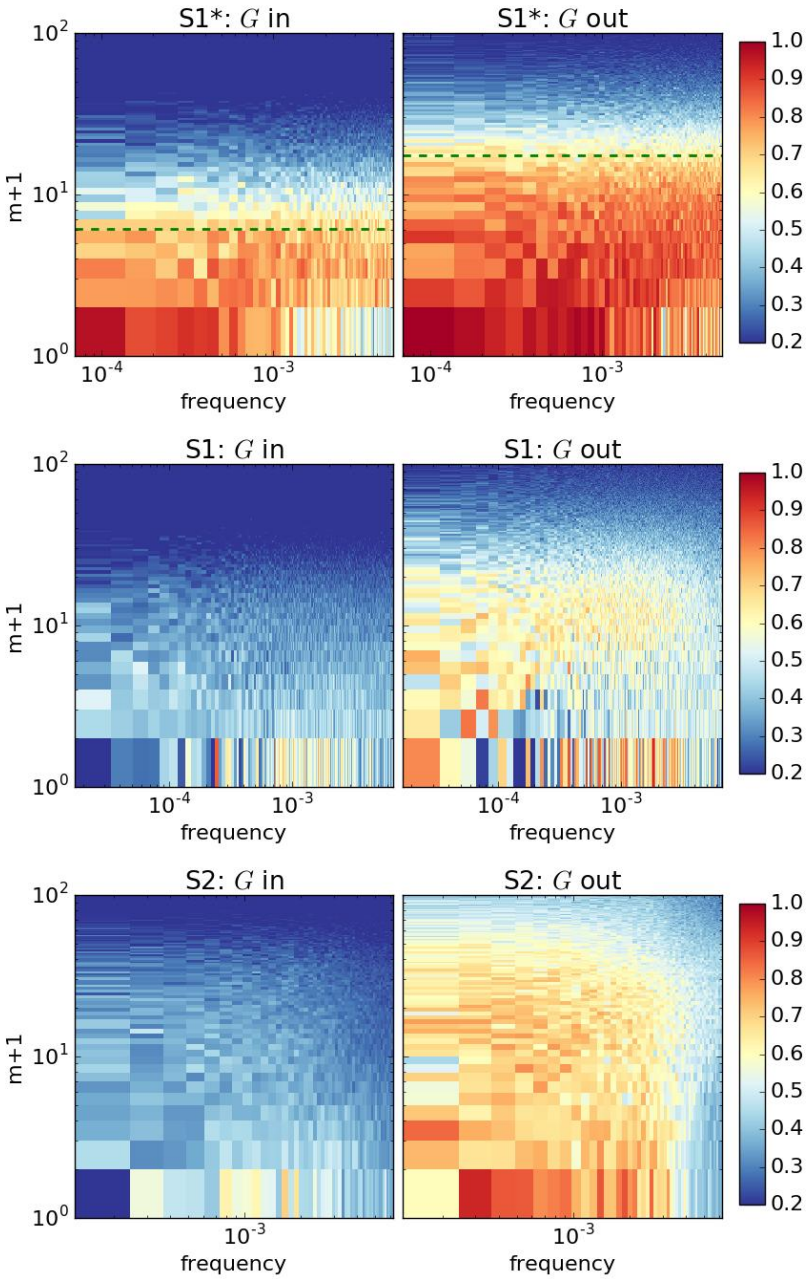

Figure 19: Colormaps of G, measuring the geostrophy of the flow, as a function of azimuthal order m and frequency, inside (left) and outside (right) the tangent cylinder. Top: simulation S1* ($E = 10^{-6}$, no magnetic field). Middle: simulation S1 ($E = 10^{-6}$, $\Lambda = 8.2$, $Le = 6.4 \times 10^{-3}$). Bottom: simulation S2 ($E = 10^{-7}$, $\Lambda = 2.5$, $Le = 1.6 \times 10^{-3}$). Frequency is in units of Ω. $G = 1$ means a geostrophic flow, $G = 0$ is for a completely ageostrophic flow. We find that for $G > 0.6$ the flow already looks fairly columnar while for $G > 0.8$ the flow displays sharp and straight columns. The dashed line indicates the wavenumber m for which $Ro_{i,o}(m) = Ro\, m/r_{i,o} = 0.1$ in S1*.

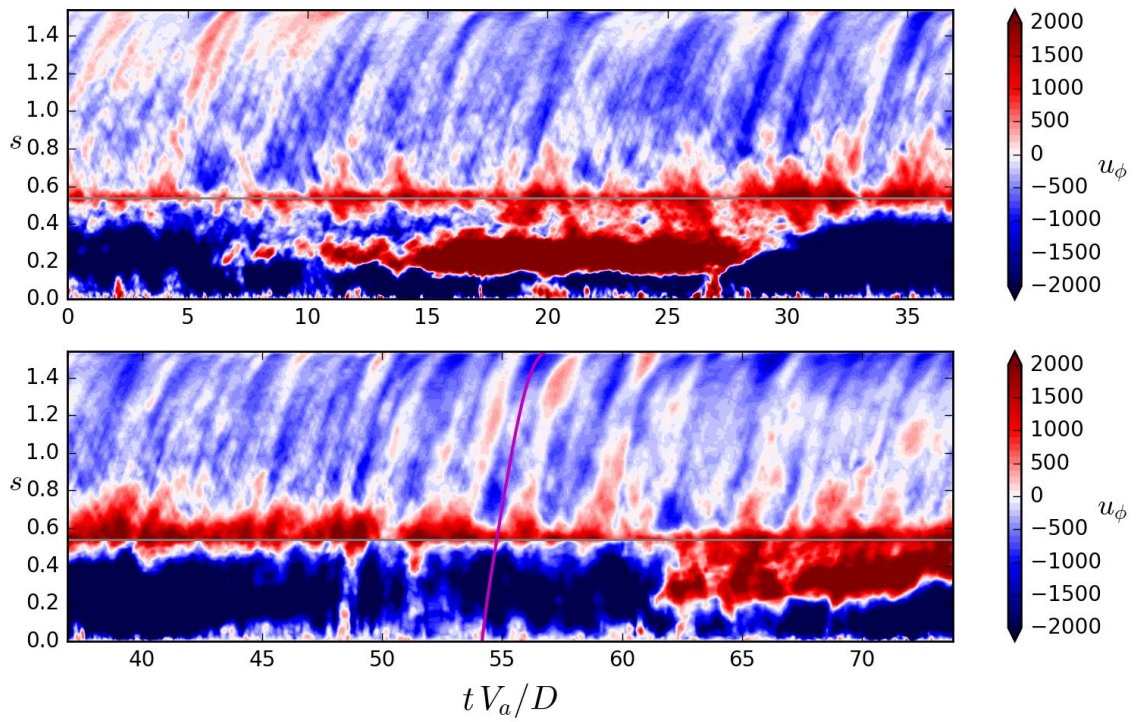

Figure 20: space-time diagram of z-averaged zonal flow u_ϕ showing torsional wave propagation outside the tangent cylinder in the simulation S2 ($E = 10^{-7}$, $Pm = 0.1$). s is the cylindrical radius, t is the magnetic diffusion time. Inside the tangent cylinder (marked by the horizontal grey line at $s = r_i$), the flow is averaged only in the northern hemisphere. The bottom panel is the continuation of the top one. The magenta curve is the signature of a propagation at the expected torsional Alfvén wave speed.

the torsional wave propagation outside the tangent cylinder without even removing the mean or employing any filtering. This contrasts with previous studies, where the mean flow was subtracted or filtered out (Wicht and Christensen, 2010; Teed et al., 2014). We also note that the frequency spectra of axisymmetric ($m = 0$) motions do not display significant peaks that would correspond to torsional modes. However, the measure of geostrophy peaks at several frequencies that are compatible with such modes (see Fig. 19 bottom right).

The torsional waves seem to originate mostly near the tangent cylinder ($s = 0.54$). Refering to figure 17, we can see that for $m = 0$, the Lorentz force dominates the region close to the inner-core (named *bli*), whereas it stays weak in the vicinity of the tangent cylinder away from the boundary (region named *tc*). This hints to the Lorentz force close to the inner-core as the main source for torsional waves, which is in line with recent findings (Teed et al., 2015).

Inside the tangent cylinder, the signal is dominated by the variability of the strong

polar vortex system, and no waves are seen there. Reflection of the waves at the equator depends on both the magnetic Prandtl number Pm (Schaeffer et al., 2012) and the mantle conductivity (Schaeffer and Jault, 2016). For an insulating mantle, only weak reflection is expected even for Pm as low as 0.1. Indeed no obvious reflection is observed in our simulations.

Figure 21 (left) represents the torsional Alfvén wave speed

$$V_a(s,t) = \sqrt{\frac{\int_z \int_\phi B_s^2 dz\, d\phi}{\int_z \int_\phi dz\, d\phi}}. \tag{12}$$

It is interesting to notice that the speed decreases towards the equator, as in Gillet et al. (2011), where it reaches a finite value about 6 times smaller than at mid-depth. The fluctuations around the mean are large inside the tangent cylinder and decrease outwards. This is consistent with the overall fluctuation level of B shown in figure 21 (right), dominated by the inner region.

3.9 Taylor constraint

We have shown that the most important terms in the vorticity equation are the Coriolis, Lorentz and Buoyancy terms, the other being much smaller. When viscosity and inertia are completely removed, Taylor (1963) showed that an equilibrium exists where the net torque on each geostrophic cylinder is zero. This is known as the Taylor constraint, leading to Taylor states. Torsional waves are triggered by deviations from this Taylor state. Following Wicht and Christensen (2010), we quantify to what extent this constraint is enforced using

$$\mathcal{T}(s,t) = \frac{\int_z \int_\phi (j \times b).e_\phi}{\int_z \left| \int_\phi (j \times b).e_\phi \right|} \tag{13}$$

which is zero if the net torque on the geostrophic cylinder of radius s is zero, and 1 if the torque at various heights is of the same sign.

Figure 22 shows different views of this quantity $\mathcal{T}$. The space-time diagram is dominated by torsional waves outside the tangent cylinder, while inside the tangent cylinder $\mathcal{T}$ is smaller. The time-average of the absolute value of $\mathcal{T}$ shows this trend as well, and also shows that $\langle|\mathcal{T}|\rangle$ decreases significantly from simulation S1 to S2. This may be linked to lower viscosity and stronger magnetic field in S2. However, the rapid increase close to the equator, which scales as $1/h(s)$ (where $h(s) = \sqrt{r_o^2 - s^2}$ is the height of the geostrophic cylinder) does not seem to change between S1 and S2. It is in fact not surprising that $\mathcal{T}$ reaches 1 near the equator. There, the height of geostrophic cylinders becomes too small for the magnetic torque to have sufficient variations in z to cancel. Hence, $\mathcal{T}$ is spoiled by geometric effects close to the equator, reaching values close to 1 independently of viscosity or inertia. Fortunately, when averaging over the volume, it will have little effect. We find $\mathcal{T}_{S1} = 0.16$ and $\mathcal{T}_{S2} = 0.12$. These numbers are significantly larger and decrease

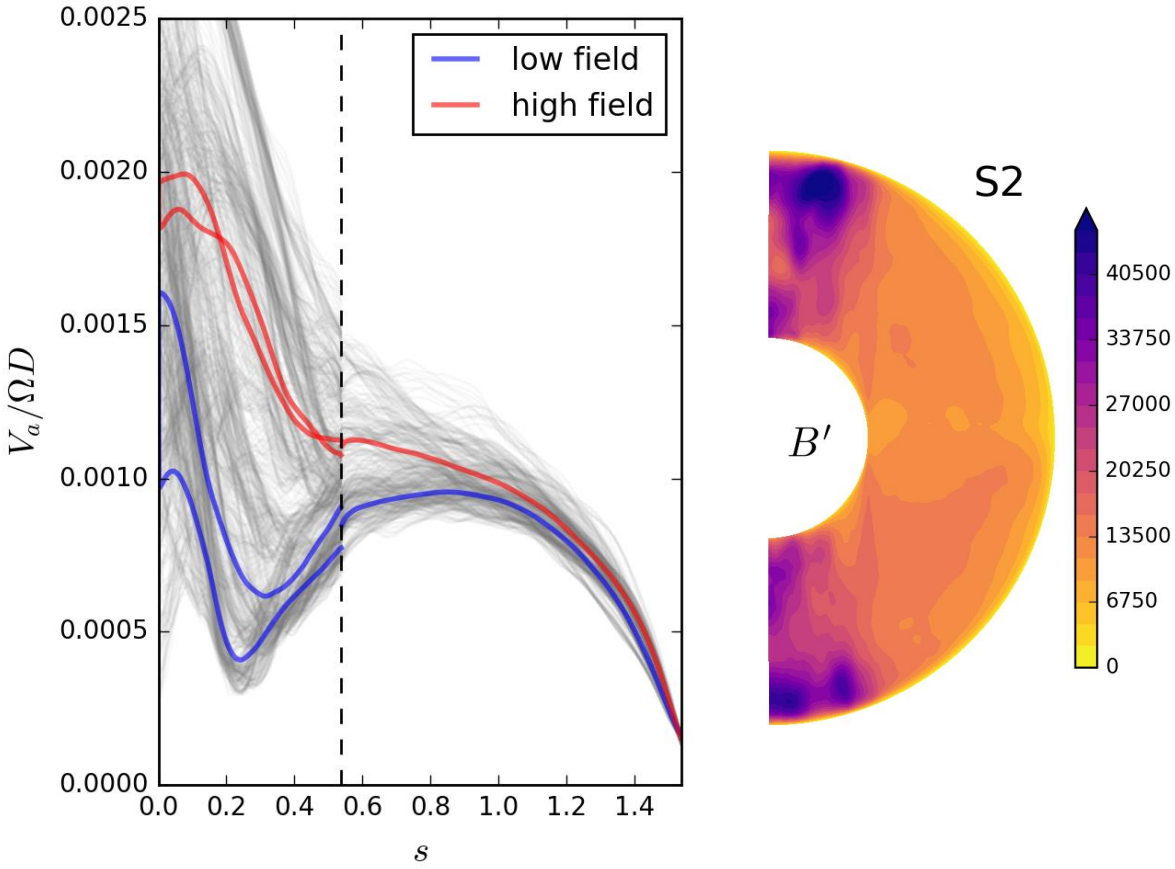

Figure 21: *Left:* rms value of the cylindrical radial magnetic field (averaged over z and ϕ) in S2, which is the inverse of the torsional Alfvén wave propagation speed. The blue and red thick curves show the time-average on the first half of the time-serie (low field) and the second half (high field). *Right:* magnetic field fluctuation levels averaged in longitude and time in S2.

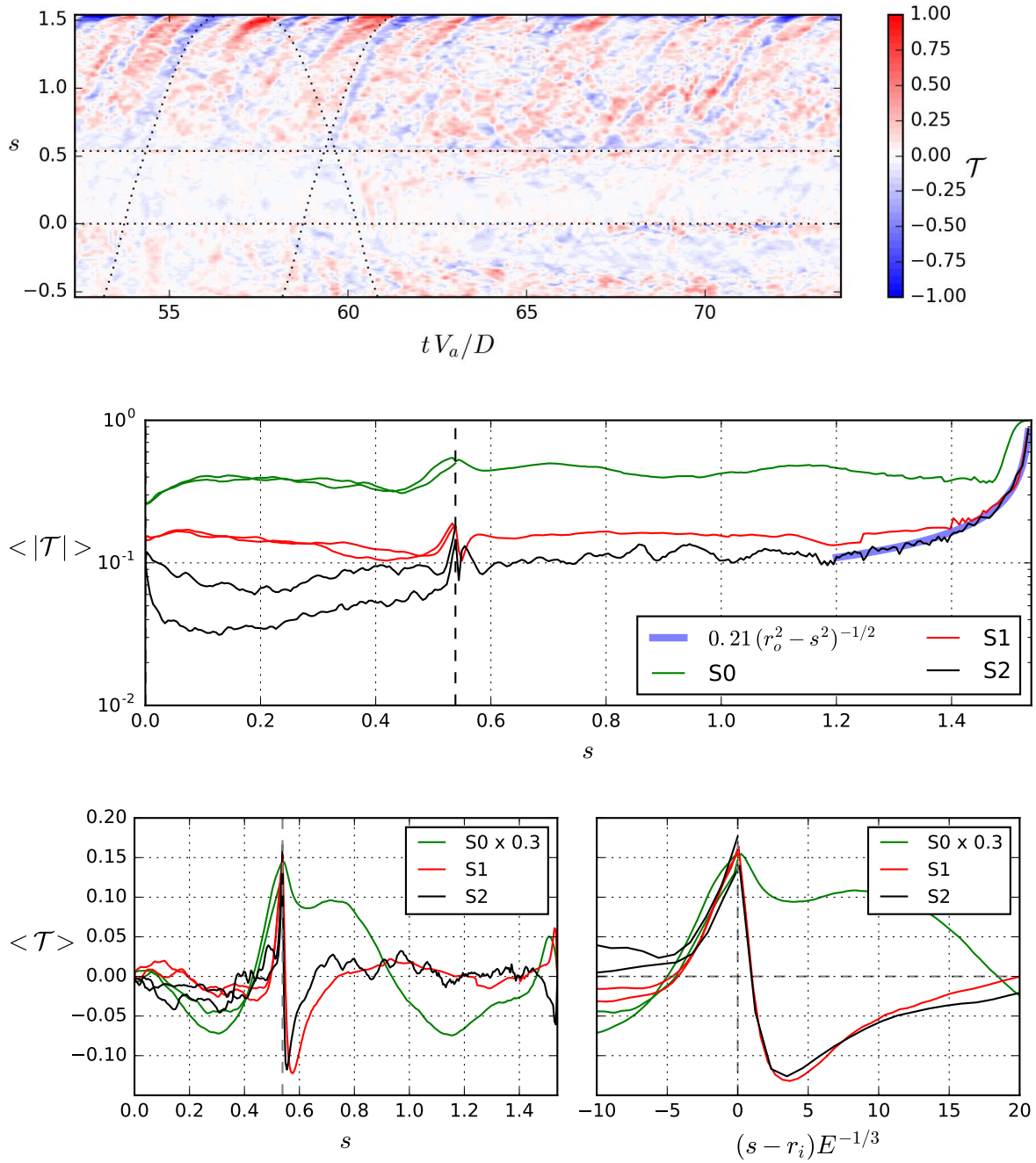

Figure 22: Distance to the Taylor constraint as measured by $\mathcal{T}$. Top: space-time diagram of $\mathcal{T}(s, z)$, in the end of simulation S2 where the signature of torsional Alfvén wave is dominant in the outer region $s > r_i$. Within the tangent cylinder ($|s| < r_i$), the values for $\mathcal{T}$ in the northern (southern) hemisphere are given for $s > 0$ ($s < 0$). Middle: time-average of the absolute value $\langle|\mathcal{T}|\rangle(s)$ for simulations S0 ($E = 10^{-5}$), S1 ($E = 10^{-6}$), and S2 ($E = 10^{-7}$). Bottom: time-average $\langle\mathcal{T}\rangle(s)$ (without the absolute value). The two lines within the tangent cylinder ($s < r_i$) are the separate values for the north and south hemispheres.

slower than those reported by Aubert et al. (2017) for stress-free boundary conditions. Considering that the Reynolds stress and viscosity in the bulk are negligible in S2, but that viscous forces balance magnetic forces near the outer boundary (see Fig. 17 *out* and *blo* regions for $m = 0$), it suggests that Ekman friction dominates the torque balance on geostrophic cylinders. Boldly extrapolating our values of $\mathcal{T}$ to the Earth's core would lead to $\mathcal{T}_{Earth} \simeq 0.01$, which might question the relevance of the magnetostrophic approach for the Earth's core.

The quantity $\langle|\mathcal{T}|\rangle$ includes contribution from torsional waves and other time-dependent fluctuations, and as such is not representative of the long-term equilibrium. We checked that the time-average of $\mathcal{T}$ (sign included) does not tend to zero but rather to very similar profiles when averaged over various time spans. These averages $\langle\mathcal{T}\rangle$ are shown for S0, S1 and S2 in Figure 22 (bottom). The amplitude is significantly smaller than that of $\langle|\mathcal{T}|\rangle$, and of the same level inside and outside the tangent cylinder.

Similar features arise in simulations S1 and S2, namely the important values near the tangent cylinder where $\mathcal{T}$ changes sign, and the rapid increase toward the equator (although with different signs). It also appears that the feature at the tangent cylinder scales as $E^{1/3}$ (or $E^{1/4}$, which are difficult to distinguish with one decade of E), pointing to an important role of viscosity there, compatible with a Stewartson layer.

4 Discussion

We have reached the milestone of $E = 10^{-7}$ for a geodynamo simulation with vigorous convection. This low viscosity associated with detailed analyses including force balances at different time- and length-scales bring a renewed picture of planetary dynamos. The internal dynamics observed in the less viscous simulation S2 is summarized in Figure 23. Importantly, global scale, axially invariant, non-zonal circulations emerge on intermediate time-scales (see Fig. 4). They result in a westward drift localized in one hemisphere (see Fig. 9). We emphasize that no heterogeneity at the boundary drive these global circulations. Instead, they arise naturally from the internal dynamics.

The zonal mean flow is strongly suppressed outside the tangent cylinder (TC), as seen in Fig. 3, where it is replaced by torsional Alfvén waves (Fig. 20) triggered by Lorentz torque fluctuations at the inner-core boundary (Fig. 17). Inside the TC, the zonal flow is enhanced by the magnetic field and takes the form of a polar twisted vortex (Fig. 3), with strong fluctuations in time (Fig. 14). Note also that the flow is by no means invariant along the rotation axis inside the TC, contrarily to the non-magnetic case. Torsional Alfvén waves are not visible in this inner region.

4.1 Heterogeneous fields

Our simulations highlight the heterogeneous nature (see Fig. 7) as well as the large temporal fluctuations (see Fig. 2) of convective spherical dynamos. The main heterogeneity is due to different dynamics separated by the tangent cylinder (TC). Albeit occupying a

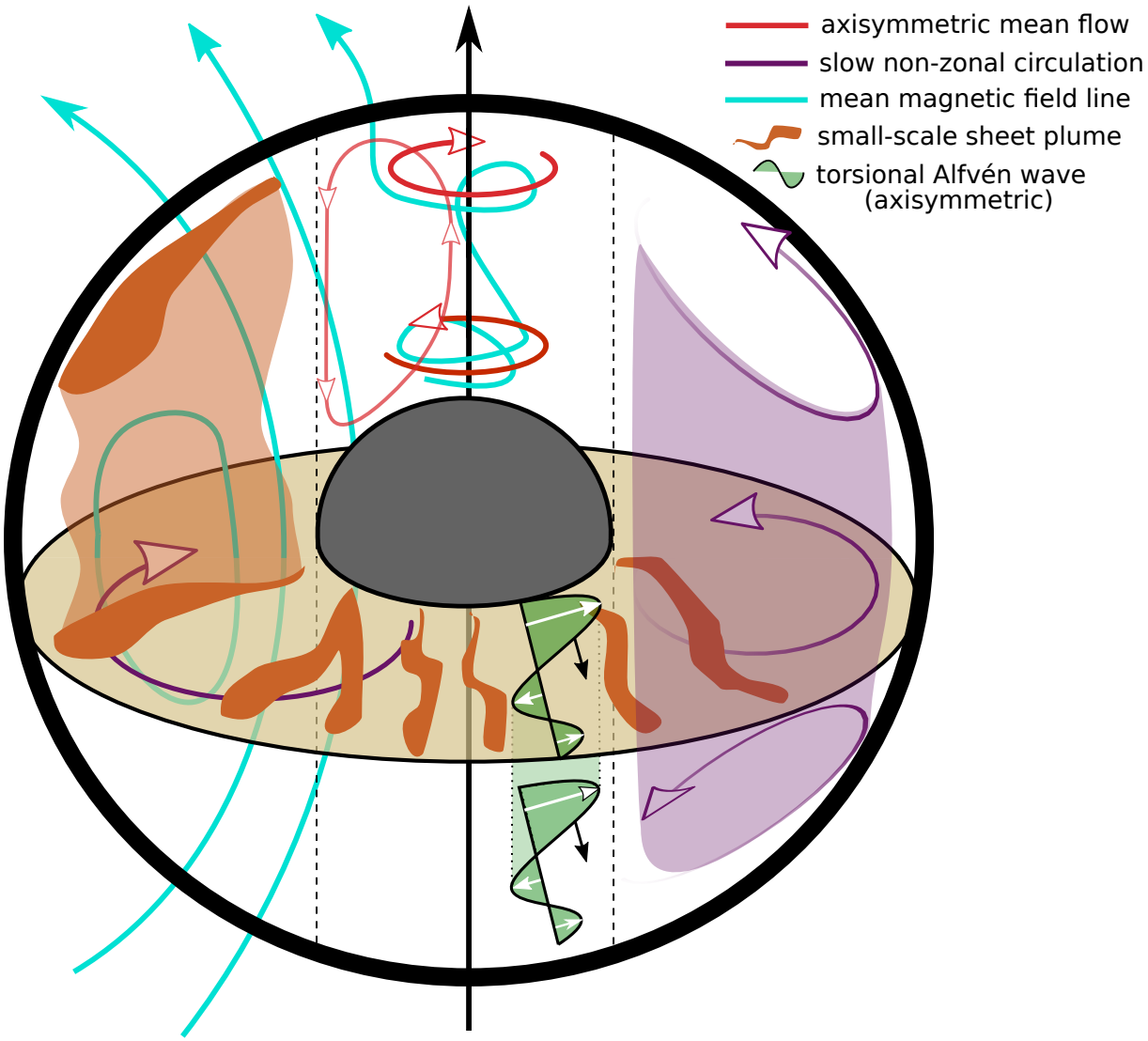

Figure 23: Sketch of the internal dynamics in our lowest viscosity simulation S2 ($E = 10^{-7}$, $Pm = 0.1$)

small volume, the region lying within the tangent cylinder exhibits strong zonal flows and toroidal fields (see Fig. 3), bearing a significant fraction of the total kinetic (about 1/10) and magnetic energies (about 1/4). These zonal flows are thermal winds driven by the density contrast between the lighter fluid inside the TC and the heavier fluid outside, as attested by our dynamical analysis (see Fig. 17 and 18). This density contrast needs attention, as it may be correlated to seismic velocity anomalies detected in the Earth's core (e.g. Souriau and Poupinet, 1990). In our simulations, the amplitude of the zonal flow and density anomaly contrast scale well according to the thermal wind balance on the global scale

$$2\Omega U \sim \frac{\delta\rho}{\rho} g. \tag{14}$$

When applied to the Earth's core ($\Omega \simeq 7 \times 10^{-5}$ s^{-1}, $U \simeq 30$ km/yr, $g \simeq 10$ m/s) it yields $\delta\rho/\rho \simeq 10^{-7}$ which is orders of magnitude too small to be detectable by seismology as such. However, seismic velocities may vary significantly with chemical composition without much density change. Such an effect may thus allow to detect a possible chemical segregation within the Earth's core akin to the one seen in our simulations. Interestingly, this segregation does not happen without magnetic field, even though the latter does not seem to enter significantly the main dynamical balance in our simulations. We note however that for the mean zonal flow within the tangent cylinder, the Lorentz force seems to slightly help the Coriolis force to counteract on the buoyancy force. It may thus be worth to study the role of magnetic forces on density segregation and how it can affect the thermal wind balance (eq. 14) in planetary cores.

It would also be interesting to study the role of these highly active polar regions for the dynamo action and for polarity reversals.

Our study also highlights the heterogeneities outside the tangent cylinder, where regions of intense magnetic fields are observed next to regions of almost zero field (see Fig. 6 and 7). This is linked to the magnetic field being mostly non-zonal (70% of the magnetic energy), especially outside the tangent cylinder. This contrasts with the field at the core surface which is mostly an axisymmetric dipole (Fig. 8). We argue that this highly heterogeneous magnetic field strength translates into heterogeneous length-scales for the convection.

Lastly, the fields are also heterogeneous in time. This aspect is mostly overlooked as most databases record time-averaged values. These large temporal fluctuations are even more intriguing as they are completely absent from our non-magnetic convection case (compare Fig. 16 with Fig. 15; see also Fig. 2).

Characteristic length-scale of convection. In previous studies, a characteristic length-scale of convection is defined by an average over the whole domain. Figure 6 shows the wide variety of length-scales present in simulation S2. It ranges from tiny plumes forming at the inner-core boundary (with measured width close to the viscous length-scale), that progressively widen while traveling across the shell. These small plumes coexist with much larger ones (Fig. 6), and even with global-scale eddies (Fig. 4). This is most likely due to the heterogeneous magnetic field, with large regions of low field next to regions of

stronger field. Hence, even though the small viscous length-scale $E^{1/3}$ is present in our simulations, the kinetic energy spectrum peaks at much larger scales (Fig. 11). In this inhomogeneous, anisotropic system, reducing the convective motion to a single length-scale would be misleading.

4.2 Comparison with Earth's core regime

Figure 24 shows tau-ell diagrams (as introduced by Nataf and Schaeffer, 2015) for what we know of the Earth's core (left) and what we can measure in simulation S2 (right). Perhaps the most striking difference concerns the length-scale for the onset of thermal convection, marked by an open black circle. For the magnetized Earth's core, this length-scale actually does not exist because the required inertial waves are replaced by Alfvén waves at these length-scales (see e.g. Galtier, 2014). For simulation S2, inertial waves can still meet the viscous scale, leading to a time-scale shorter than any magnetic or advective time-scale. This may explain why the viscous length-scale $\sim E^{1/3}$ associated with the onset of thermal convection is present in S2 (as in most other simulations) despite the seemingly strong magnetic field. Overcoming this while still keeping rotation dominant requires

$$1 \gg Le > E^{1/3} \tag{15}$$

or translated in terms of Elsasser number Λ,

$$\Lambda > Pm\, E^{-1/3}. \tag{16}$$

When searching in the available databases for such simulations (the ones represented in Fig. 1), no simulation matches simultaneously the following three criteria: $A < 1$, $Pm < 1$, $Le > E^{1/3}$.

Also apparent on Figure 24, is that local $Rm(\ell) = 1$ (intersection of thick red line with blue dashed line) occurs at quite large scales, and corresponds to the start of decaying magnetic energy, as seen in Fig. 11.

We also remark a last discrepancy between Earth's core and S2: the kinetic energy of the surface flow and the magnetic energy at the surface are not in the same ordering.

Despite having many appealing features, we thus argue that our most demanding simulation – just as any other from several databases – has not yet reached a regime where all relevant time- and length-scales are ordered as in the Earth's core.

Influence of the magnetic field. Although the force balance suggests a mild effect of the magnetic field, this is clearly not the case. As shown in figure 2, when the magnetic field is turned off (everything else being kept the same), the kinetic energy quickly increases by a factor 10. One also observes that the convection is more evenly distributed in the whole shell, with the formation of a strong zonal jet outside the tangent cylinder, instead of a strong polar vortex in the dynamo case (see figures 3, 5). Surprisingly, the non-magnetic convection is also largely invariant along the rotation axis inside the TC (Fig. 19).

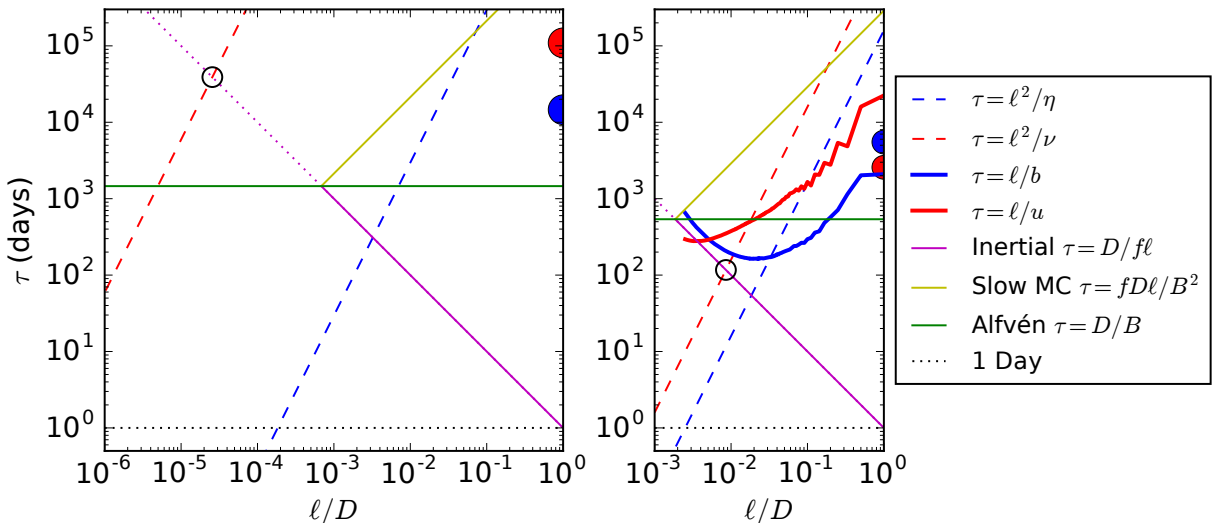

Figure 24: Tau-ell diagrams for the Earth's core (left) and simulation S2 (right). ℓ is here the length scale, and τ the time-scale, while $f = \Omega/2\pi$ is the rotation rate. Time needed for several types of wave to cross the core are displayed as a function of the wave length ℓ. The viscous and magnetic diffusion time-scales are also represented as dashed lines. The onset of (non-magnetic) thermal convection happens at the intersection between the inertial wave time-scale and the viscous time-scale, marked by a black circle. Spectra from S2 are translated into time- and length-scales and plotted as thick lines. The observed surface core flow (magnetic field) is marked by the big red (blue) filled circle.

In the presence of magnetic fields, the flows are organized to limit induction, by aligning magnetic and velocity field where possible. In this way, the strong magnetic field obtained in S1 and S2 completely changes the flow. Not only does it completely suppress the geostrophic jets, but the convective plumes extend further in the shell (because they are not blocked by the zonal jets anymore). The plumes are also of larger scale in the bulk, but the convection often starts at very small scale at the ICB, even smaller than without magnetic field. Matsui et al. (2014) report that when going to larger forcing, the effect of the magnetic field on the small scale of convection seems to be lost, in agreement to our findings.

Outside the TC, the flow is mostly axially invariant at large time- and length-scales. But this is not the case inside the TC, where the axial invariance of the flow is destroyed. There, the mean magnetic field has Elsasser number $\Lambda_0 \simeq 1$, and is largely aligned with the mean flow, limiting the amount of induction.

Perspectives and future work. Our direct simulations may serve as benchmarks for developing large eddy simulations schemes (see e.g. Buffett, 2003; Nataf and Schaeffer, 2015; Aubert et al., 2017) and for validating asymptotic models (e.g. Calkins et al., 2016), which are both needed to further progress towards realistic dynamos. Several terabytes of data will be held available for a few years to allow further analysis. It would be also instructive to characterize the turbulence and the dynamo mechanism. Our analysis suggests that a strong omega effect within the tangent cylinder might be coupled to an alpha effect outside. The increase of relative helicity with decreasing Ekman number (Fig. 10) shows that this picture is robust and does not rely on Ekman pumping. (Calkins et al., 2016) have recently emphasized the significance of the ordinary Prandtl number in the selection of the dynamo mechanism in a rotating layer. We also have to investigate whether our results hold for $Pr \neq 1$.

Because of the apparently important role played by the tangent cylinder (TC), it would be of great interest to revisit the role of a conducting inner-core in this parameter range. Indeed, it might enable the strong toroidal field to reach the boundary and alter the scale of the plumes originating there. More importantly, if the dynamics within the TC are important, we should compare dynamos with and without inner-core, the latter having relevance for the early Earth or other planets. It may also be interesting to isolate the region within the tangent cylinder to study its own dynamics decoupled from the outer region.

Our findings also question the relevance of the magnetostrophic approach for planetary dynamos. Indeed, the measure $\mathcal{T}$ seems to decrease very slowly with the Ekman number, suggesting a significant role of the Ekman friction, which may not be negligible even at Earth's core conditions.

Acknowledgements

The XSHELLS, SHTns and SINGE codes used in this paper are freely available at `https://bitbucket.org/nschaeff`. We acknowledge PRACE and GENCI for awarding us access to resource Curie based in France at TGCC (grant pa1413 and t2014047258); GENCI awarded further access to Occigen (CINES) and Turing (IDRIS) under grant x2015047382 and x2016047382. Part of the computations were also performed on the Froggy platform of CIMENT (`https://ciment.ujf-grenoble.fr`), supported by the Rhône-Alpes region (CPER07_13 CIRA), OSUG@2020 LabEx (ANR10 LABX56) and Equip@Meso (ANR10 EQPX-29-01). Heavy data post-processing was partly performed on the S-CAPAD platform, IPGP, France. This work was funded by the French *Agence Nationale de la Recherche* under grants ANR-11-BS56-011 (AVSGeomag), ANR-13-BS06-0010 (TuDy) and ANR-14-CE33-0012 (MagLune). ISTerre is part of Labex OSUG@2020 (ANR10 LABX56). All figures were produced using matplotlib (`http://matplotlib.org/`) except Fig. 7 rendered with paraview (`http://www.paraview.org/`) and Fig. 23, drawn with inkscape (`https://inkscape.org/`).

References

Aubert, J., 2005. Steady zonal flows in spherical shell dynamos. Journal of Fluid Mechanics 542, 53–67.

Aubert, J., Finlay, C. C., Fournier, A., Oct. 2013. Bottom-up control of geomagnetic secular variation by the earth's inner core. Nature 502 (7470), 219–223.
URL `http://dx.doi.org/10.1038/nature12574`

Aubert, J., Gastine, T., Fournier, A., 2017. Spherical convective dynamos in the rapidly rotating asymptotic regime. Journal of Fluid Mechanics.
URL `https://arxiv.org/abs/1611.04776`

Aubert, J., Labrosse, S., Poitou, C., Dec. 2009. Modelling the palaeo-evolution of the geodynamo. Geophysical Journal International 179 (3), 1414–1428.
URL `http://dx.doi.org/10.1111/j.1365-246x.2009.04361.x`

Aujogue, K., Pothérat, A., Sreenivasan, B., 2015. Onset of plane layer magnetoconvection at low ekman number. Physics of Fluids (1994-present) 27 (10), 106602.

Bouligand, C., Gillet, N., Jault, D., Schaeffer, N., Fournier, A., Aubert, J., 2016. Frequency spectrum of the geomagnetic field harmonic coefficients from dynamo simulations. Geophysical Journal International 207 (2), 1142–1157.

Braginsky, S. I., Roberts, P. H., 1995. Equations governing convection in earth's core and the geodynamo. Geophysical & Astrophysical Fluid Dynamics 79 (1-4), 1–97.

Buffett, B. A., 2003. A comparison of subgrid-scale models for large-eddy simulations of convection in the earth's core. Geophysical Journal International 153 (3), 753–765.
URL http://dx.doi.org/10.1046/j.1365-246X.2003.01930.x

Busse, F. H., Apr. 1975. A model of the geodynamo. Geophysical Journal of the Royal Astronomical Society 42 (2), 437–459.
URL http://dx.doi.org/10.1111/j.1365-246X.1975.tb05871.x

Calkins, M. A., Julien, K., Tobias, S. M., Aurnou, J. M., Marti, P., 2016. Convection-driven kinematic dynamos at low rossby and magnetic prandtl numbers: Single mode solutions. Physical Review E 93 (2), 023115.

Chandrasekhar, S., 1961. Hydrodynamics and Hydrodynamic Stability, Clarendon. Oxford.

Cheng, J., Aurnou, J., 2016. Tests of diffusion-free scaling behaviors in numerical dynamo datasets. Earth and Planetary Science Letters 436, 121–129.

Christensen, U. R., 2010. Dynamo scaling laws and applications to the planets. Space science reviews 152 (1), 565–590.

Christensen, U. R., Aubert, J., 2006. Scaling properties of convection-driven dynamos in rotating spherical shells and application to planetary magnetic fields. Geophysical Journal International 166 (1), 97–114.
URL http://dx.doi.org/10.1111/j.1365-246x.2006.03009.x

Christensen, U. R., Aubert, J., Cardin, P., Dormy, E., Gibbons, S., Glatzmaier, G. A., Grote, E., Honkura, Y., Jones, C., Kono, M., Matsushima, M., Sakuraba, A., Takahashi, F., Tilgner, A., Wicht, J., Zhang, K., Dec. 2001. A numerical dynamo benchmark. Physics of The Earth and Planetary Interiors 128 (1-4), 25–34.
URL http://dx.doi.org/10.1016/s0031-9201(01)00275-8

Christensen, U. R., Aubert, J., Hulot, G., Aug. 2010. Conditions for earth-like geodynamo models. Earth and Planetary Science Letters 296 (3-4), 487–496.
URL http://dx.doi.org/10.1016/j.epsl.2010.06.009

Christensen, U. R., Holzwarth, V., Reiners, A., 2009. Energy flux determines magnetic field strength of planets and stars. Nature 457 (7226), 167–169.

Davidson, P., 2014. The dynamics and scaling laws of planetary dynamos driven by inertial waves. Geophysical Journal International 198 (3), 1832–1847.
URL http://gji.oxfordjournals.org/content/198/3/1832.abstract

Dormy, E., 2016. Strong-field spherical dynamos. Journal of Fluid Mechanics 789, 500–513.

Finlay, C. C., Jackson, A., 2003. Equatorially dominated magnetic field change at the surface of earth's core. Science 300 (5628), 2084–2086.

Fournier, A., Aubert, J., Thebault, E., Schaeffer, N., Apr. 2012. A database of synthetic observations for geomagnetic data assimilation practice. In: Abbasi, A., Giesen, N. (Eds.), EGU General Assembly Conference Abstracts. Vol. 14 of EGU General Assembly Conference Abstracts. p. 6243.

Galtier, S., Oct. 2014. Weak turbulence theory for rotating magnetohydrodynamics and planetary flows. Journal of Fluid Mechanics 757, 114–154.
URL http://dx.doi.org/10.1017/jfm.2014.490

Gillet, N., Jault, D., Canet, E., Fournier, A., 2010. Fast torsional waves and strong magnetic field within the earth's core. Nature 465 (7294), 74–77.
URL http://dx.doi.org/10.1038/nature09010

Gillet, N., Jault, D., Finlay, C. C., 2015. Planetary gyre, time-dependent eddies, torsional waves, and equatorial jets at the earth's core surface. Journal of Geophysical Research: Solid Earth 120 (6), 3991–4013.

Gillet, N., Schaeffer, N., Jault, D., 2011. Rationale and geophysical evidence for quasi-geostrophic rapid dynamics within the earth's outer core. Physics of the Earth and Planetary Interiors 187 (3), 380–390.
URL http://dx.doi.org/10.1016/j.pepi.2012.03.006

Glatzmaier, G., Roberts, P., 1995. A three-dimensional self-consistent computer simulation of a geomagnetic field reversal. Nature 377 (6546), 203–209.

Grooms, I., Julien, K., Weiss, J. B., Knobloch, E., 2010. Model of convective taylor columns in rotating rayleigh-bénard convection. Physical review letters 104 (22), 224501.

Hori, K., Wicht, J., Christensen, U., 2012. The influence of thermo-compositional boundary conditions on convection and dynamos in a rotating spherical shell. Physics of the Earth and Planetary Interiors 196, 32–48.

Jault, D., Finlay, C., 2015. Waves in the core and mechanical core-mantle interactions. In: Treatise on Geophysics. Elsevier Science.

Jones, C. A., 2008. Course 2 dynamo theory. In: Cardin, P., Cugliandolo, L. (Eds.), Dynamos. Vol. 88 of Les Houches. Elsevier, pp. 45 – 135.
URL http://www.sciencedirect.com/science/article/pii/S0924809908800066

Kageyama, A., Miyagoshi, T., Sato, T., Aug. 2008. Formation of current coils in geodynamo simulations. Nature 454 (7208), 1106–1109.
URL http://dx.doi.org/10.1038/nature07227

King, E. M., Buffett, B. A., 2013. Flow speeds and length scales in geodynamo models: The role of viscosity. Earth and Planetary Science Letters 371, 156–162.
URL http://dx.doi.org/10.1016/j.epsl.2013.04.001

Labbé, F., Jault, D., Gillet, N., 2015. On magnetostrophic inertia-less waves in quasi-geostrophic models of planetary cores. Geophysical & Astrophysical Fluid Dynamics 109 (6), 587–610.

Livermore, P. W., Hollerbach, R., Jackson, A., 2013. Electromagnetically driven westward drift and inner-core superrotation in earth's core. Proceedings of the National Academy of Sciences 110 (40), 15914–15918.

Matsui, H., Heien, E., Aubert, J., Aurnou, J. M., Avery, M., Brown, B., Buffett, B., Busse, F., Christensen, U., Davies, C., Featherstone, N., Gastine, T., Glatzmaier, G., Gubbins, D., Guermond, J.-L., Hayashi, Y.-Y., Hollerbach, R., Hwang, L., Jackson, A., Jones, C., Jiang, W., Kellogg, L., Kuang, W., Landeau, M., Marti, P., Olson, P., Ribeiro, A., Sasaki, Y., Schaeffer, N., Simitev, R., Sheyko, A., Silva, L., Stanley, S., Takahashi, F., Takehiro, S., Wicht, J., Willis, A., 2016. Performance benchmarks for a next generation numerical dynamo model. Geochemistry, Geophysics, Geosystems 17 (5), 1586–1607.
URL http://dx.doi.org/10.1002/2015GC006159

Matsui, H., King, E., Buffett, B., 2014. Multiscale convection in a geodynamo simulation with uniform heat flux along the outer boundary. Geochemistry, Geophysics, Geosystems 15 (8), 3212–3225.
URL http://dx.doi.org/10.1002/2014GC005432

Moffatt, H. K., 1978. Field Generation in Electrically Conducting Fluids. Cambridge University Press, Cambridge, London, New York, Melbourne.

Monchaux, R., Berhanu, M., Aumaître, S., Chiffaudel, A., Daviaud, F., Dubrulle, B., Ravelet, F., Fauve, S., Mordant, N., Pétrélis, F., et al., 2009. The von kármán sodium experiment: turbulent dynamical dynamos. Physics of Fluids (1994-present) 21 (3), 035108.

Nataf, H.-C., Schaeffer, N., 2015. 8.06 - turbulence in the core. In: Schubert, G. (Ed.), Treatise on Geophysics (Second Edition), second edition Edition. Elsevier, Oxford, pp. 161 – 181.
URL http://dx.doi.org/10.1016/B978-0-444-53802-4.00142-1

Olson, P., Aurnou, J., 1999. A polar vortex in the earth's core. Nature 402 (6758), 170–173.

Oruba, L., Dormy, E., 2014. Predictive scaling laws for spherical rotating dynamos. Geophysical Journal International 198 (2), 828–847.

Pais, M., Jault, D., 2008. Quasi-geostrophic flows responsible for the secular variation of the earth's magnetic field. Geophysical Journal International 173 (2), 421–443.

Pais, M. A., Morozova, A. L., Schaeffer, N., 2015. Variability modes in core flows inverted from geomagnetic field models. Geophysical Journal International 200 (1), 402–420.
URL http://dx.doi.org/10.1093/gji/ggu403

Sakuraba, A., Roberts, P. H., Oct. 2009. Generation of a strong magnetic field using uniform heat flux at the surface of the core. Nature Geoscience 2 (11), 802–805.
URL http://dx.doi.org/10.1038/ngeo643

Schaeffer, N., Mar. 2013. Efficient spherical harmonic transforms aimed at pseudospectral numerical simulations. Geochem. Geophys. Geosyst. 14 (3), 751–758.
URL http://arxiv.org/abs/1202.6522

Schaeffer, N., Cardin, P., May 2006. Quasi-geostrophic kinematic dynamos at low magnetic prandtl number. Earth and Planetary Science Letters 245 (3-4), 595–604.
URL http://dx.doi.org/10.1016/j.epsl.2006.03.024

Schaeffer, N., Jault, D., 2016. Electrical conductivity of the lowermost mantle explains absorption of core torsional waves at the equator. Geophysical Research Letters 43 (10), 4922–4928.
URL http://dx.doi.org/10.1002/2016GL068301

Schaeffer, N., Jault, D., Cardin, P., Drouard, M., 2012. On the reflection of alfvén waves and its implication for earth's core modeling. Geophysical Journal International 191 (2), 508–516.
URL http://dx.doi.org/10.1111/j.1365-246X.2012.05611.x

Schaeffer, N., Pais, M. A., 2011. On symmetry and anisotropy of earth-core flows. Geophysical Research Letters 38 (10).
URL http://dx.doi.org/10.1029/2011GL046888

Sheyko, A., 2014. Numerical investigations of rotating mhd in a spherical shell. Ph.D. thesis, ETH-Zürich.
URL http://dx.doi.org/10.3929/ethz-a-010198511

Soderlund, K. M., King, E. M., Aurnou, J. M., Jun. 2012. The influence of magnetic fields in planetary dynamo models. Earth and Planetary Science Letters 333-334, 9–20.
URL http://dx.doi.org/10.1016/j.epsl.2012.03.038

Souriau, A., Poupinet, G., 1990. A latitudinal pattern in the structure of the outermost liquid core, revealed by the travel times of skks-sks seismic phases. Geophysical Research Letters 17 (11), 2005–2007.
URL http://dx.doi.org/10.1029/GL017i011p02005

Sreenivasan, B., Jones, C. A., 2006. Azimuthal winds, convection and dynamo action in the polar regions of planetary cores. Geophysical and Astrophysical Fluid Dynamics 100 (4-5), 319–339.

Sreenivasan, B., Jones, C. A., 2011. Helicity generation and subcritical behaviour in rapidly rotating dynamos. Journal of Fluid Mechanics 688, 5–30.
URL http://dx.doi.org/10.1017/jfm.2011.233

Stewartson, K., 1966. On almost rigid rotations. part 2. Journal of Fluid Mechanics 26 (01), 131–144.
URL http://dx.doi.org/10.1017/s0022112066001137

Takahashi, F., Shimizu, H., May 2012. A detailed analysis of a dynamo mechanism in a rapidly rotating spherical shell. Journal of Fluid Mechanics 701, 228–250.
URL http://dx.doi.org/10.1017/jfm.2012.154

Taylor, J., 1963. The magneto-hydrodynamics of a rotating fluid and the earth's dynamo problem. In: Proceedings of the Royal Society of London A: Mathematical, Physical and Engineering Sciences. Vol. 274. The Royal Society, pp. 274–283.

Teed, R. J., Jones, C. A., Tobias, S. M., 2014. The dynamics and excitation of torsional waves in geodynamo simulations. Geophysical Journal International 196 (2), 724–735.

Teed, R. J., Jones, C. A., Tobias, S. M., 2015. The transition to earth-like torsional oscillations in magnetoconvection simulations. Earth and Planetary Science Letters 419, 22–31.

Vidal, J., Schaeffer, N., 2015. Quasi-geostrophic modes in the earth's fluid core with an outer stably stratified layer. Geophysical Journal International 202 (3), 2182–2193.
URL http://dx.doi.org/10.1093/gji/ggv282

Wicht, J., Christensen, U. R., 2010. Torsional oscillations in dynamo simulations. Geophysical Journal International 181 (3), 1367–1380.

Wu, C.-C., Roberts, P. H., JAN 2 2015. On magnetostrophic mean-field solutions of the geodynamo equations. Geophysical & Astrophysical Fluid Dynamics 109 (1), 84–110.

Yadav, R. K., Gastine, T., Christensen, U. R., Duarte, L., Reiners, A., 2016a. Effect of shear and magnetic field on the heat-transfer efficiency of convection in rotating spherical shells. Geophysical Journal International 204 (2), 1120–1133.

Yadav, R. K., Gastine, T., Christensen, U. R., Wolk, S. J., Poppenhaeger, K., 2016b. Approaching a realistic force balance in geodynamo simulations. Proceedings of the National Academy of Sciences 113 (43), 12065–12070.
URL http://dx.doi.org/10.1073/pnas.1608998113